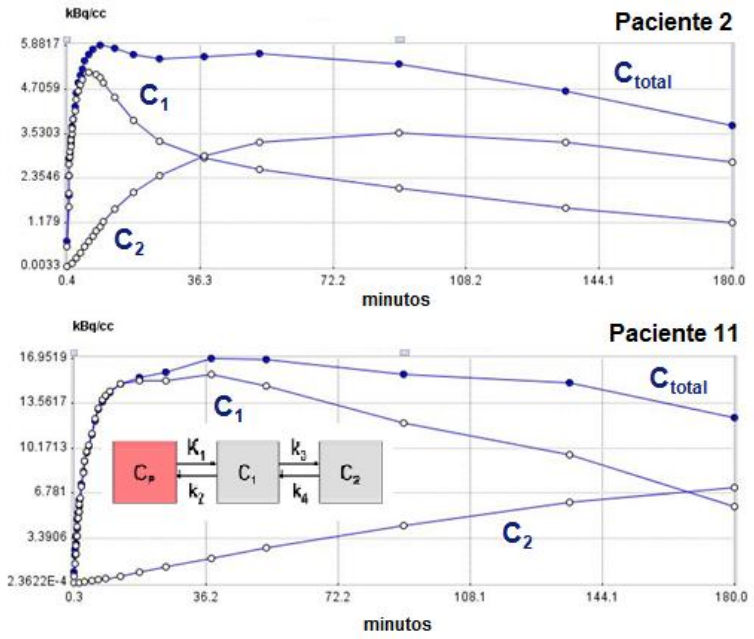


# Clinical dosimetry and pharmacokinetic modelling of radiolabeled Sarabesin 3 with $^{68}$Ga and $^{177}$Lu: A new approach for prostate cancer theranostics


## Ana Rita Carvalho Teixeira

**Mestrado em Física Médica**
Departamento de Física e Astronomia
2019

**Orientador**
João António Miranda dos Santos, PhD
Assessor de Saúde (Física Médica) no Instituto Português de Oncologia Francisco Gentil, EPE;
Professor Afiliado da Universidade do Porto (ICBAS)

**Coorientador**
Mark W. Konijnenberg, PhD
Físico Médico no Departamento de Medicina Nuclear do Erasmus MC, Roterdão


Todas as correções determinadas pelo júri, e só essas, foram efetuadas.

O Presidente do Júri,

Porto, _____/_____/_____

# Acknowledgements

First of all, I would like to express my deepest heartfelt appreciation to Mark Konijnenberg for his extraordinary patience, motivation and guidance through all this research work.

A word of gratitude also to Ingrid Bakker for sharing her expertise and for trusting me to colaborate with her in this study.

Discussions with Marcel Segbers have also been insightful, thus my word of appreciation goes for him too.

A special thanks to Professor Marion de Jong for the opportunity of doing this internship and for all her kindness.

Furthermore, I am also extremely grateful to the all the SPECTRIM group for all the support and for making this experience one of the best and most rewarding of my life.

This work would not have been possible without the encouragment and counselling of Professor João Santos. Thank you.

A word of appreciation to my boyfriend and my friends should not be forgotten for always believing in me and for inspiring me to achieve my goals.

Finally and above all else, I would like to thank my parents for allowing me the opportunity to persue my dreams and for their unconditional love and support throughout my life. I am very lucky for the marvelous family we share. Thank you.

# Abstract

At the present time, primary diagnosis of prostate cancer involves taking biopsies of the prostate, which are proven to be very invasive and unpleasant for the patients. The radiopharmaceutical [$^{68}$Ga]SB3 is here presented as an alternative for diagnosing prostate cancer through PET/CT imaging. SB3 is a bombesin analogue and a gastrin-releasing peptide receptor (GRPR) antagonist, which highlights the potential of this tracer, since early stage prostatic carcinomas are known for overexpressing GRPR and presenting high affinity for bombesin analogues. Moreover, SB3 can also be labelled with $^{177}$Lu for therapeutic purposes, which immediately suggests a theranostic approach.

The present work is based on a clinical study involving 11 patients with prostate cancer confined to the primary organ that underwent a PET/CT scan with [$^{68}$Ga]SB3. The goal was to estimate the dosimetry of this radiotracer, as well as its pharmacokinetic behaviour from the application of compartmental models. It was also analysed the possibility of using [$^{177}$Lu]SB3 as a therapeutic agent, along with the potential of using the $^{68}$Ga images to predict the therapy response.

Time-activity curves in multiple organs were fitted and integrated to obtain the absorbed doses. It was predicted the decay of $^{177}$Lu from the $^{68}$Ga curves for the organs at risk and calculated the respective absorbed doses. Compartmental models were applied to the data of 2 patients, based on activity curves of the blood, the tumour and the normal prostate. The parameters of each model along with the concentrations in each compartment allowed us to predict the tracer behaviour when labelled with $^{177}$Lu and decide if the therapy would be favourable in each case. It was also evaluated the absorbed dose in one of the tumours.

The highest uptake of the radiotracer was verified in the pancreas, followed by the kidneys (pelvis) and urinary bladder, whose estimated doses were 198 $\mu$Gy/MBq, 133 $\mu$Gy/MBq and 115 $\mu$Gy/MBq, respectively. The effective dose 103 of [$^{68}$Ga]SB3 is 13 $\mu$Sv/MBq. The therapeutic doses per cycle are at a maximum of 4.7 Gy, 5.5 Gy, 22.9 Gy e 0.4 Gy for the pancreas, kidneys (cortex and pelvis) and red bone marrow assuming 7.4 GBq of administered activity. It was verified for PT2 that the specific binding of [$^{68}$Ga]SB3 to the tumour was decreasing after 90 min. On the other hand, this binding seemed to increase gradually in PT11. His tumour is expected to receive a dose of 14.1 Gy per cycle, considering partial volume effects.

In conclusion, the effective dose of [$^{68}$Ga]SB3 is similar to the effective doses of the most common PET tracers currently used. The estimated absorbed doses in the organs at risk do not yield significant toxicity (diagnostic and therapy). Compartmental modelling seems to be a good method to select patients for therapy. However, it strongly relies on the quality of the input curves. Finally, for patient 11, the estimated [$^{177}$Lu]SB3 absorbed dose may not be enough to treat the tumour, which demonstrates the importance of the pre-treatment dosimetry.

**Keywords:** Gastrin-releasing peptide receptor antagonist; PET/CT; Theranostics; Dosimetry; Pharmacokinetics; Compartmental Modelling; Prostate Cancer

# Resumo

Atualmente, o diagnóstico primário do cancro da próstata envolve a realização de biopsias da próstata, um método que já demonstrou ser bastante invasivo e desconfortável para os pacientes. O radiofármaco [$^{68}$Ga]SB3 é aqui apresentado como alternativa ao diagnóstico do cancro da próstata a partir de imagens de PET/CT. SB3 é um análogo da bombesina e um antagonista dos recetores GRP. Estas características realçam o potencial deste fármaco, dado que carcinomas primários da próstata são conhecidos pela presença significativa de recetores GRP e por apresentarem grande afinidade com análogos da bombesina. Além disso, SB3 pode ser marcado radioativamente com $^{177}$Lu para aplicações terapêuticas, o que sugere imediatamente uma abordagem teranóstica.

Este trabalho baseia-se num estudo clínico que envolve 11 pacientes com cancro da próstata confinado ao órgão primário e que realizaram um exame de PET/CT com [$^{68}$Ga]SB3. Os objetivos foram aceder à dosimetria e ao seu comportamento farmacocinético pela aplicação de modelos compartimentais. Foi ainda analisada a possibilidade de utilizar [$^{177}$Lu]SB3 como agente terapêutico e o potencial de usar as imagens de $^{68}$Ga para prever a resposta à terapia.

O fitting e integração das curvas de atividade de [$^{68}$Ga]SB3 em vários órgaõs levaram à obtenção das doses absorvidas. Foi estimado o decaimento do $^{177}$Lu a partir das curvas de $^{68}$Ga nos órgãos de risco e calculadas as respetivas doses absorvidas. Através das curvas de uptake no sangue, tumor e próstata saudável, foram aplicados modelos compartimentais a 2 pacientes. Os parâmetros dos modelos e as concentrações em cada compartimento permitiram prever o comportamento do fármaco quando marcado com $^{177}$Lu e decidir se a terapia seria favorável em cada caso. Foi estimada a dose absorvida num tumor particular.

O pâncreas é o órgão com maior captação do fármaco, seguido pelos rins (pélvis) e bexiga, cujas doses estimadas foram de 198 $\mu$Gy/MBq, 133 $\mu$Gy/MBq e 115 $\mu$Gy/MBq, respetivamente. A dose efetiva 103 de [$^{68}$Ga]SB3 é de 13 $\mu$Sv/MBq. As doses terapêuticas por ciclo serão, no máximo, de 4.7 Gy, 5.5 Gy, 22.9 Gy e 0.4 Gy para o pâncreas, rins (córtex e pélvis) e medula óssea (para 7.4 GBq administrados). Verificou-se que, para o paciente 2, a ligação específica de [$^{68}$Ga]SB3 ao tumor diminuía ao fim de 90 min. Já para o paciente 11, parecia aumentar progressivamente. Espera-se que o seu tumor receba uma dose de 14.1 Gy por ciclo, considerando efeitos de volume parcial.

Em suma, [$^{68}$Ga]SB3 apresenta uma dose efetiva semelhante à dos compostos usados hoje em medicina nuclear. A dose estimada para os órgãos de risco (diagnóstico e terapia) não se traduz numa toxicidade significativa. A aplicação de modelos compartimentais revelou-se um bom método para selecionar os pacientes para terapia, embora bastante dependente da qualidade das curvas utilizadas. Verificou-se que, para o paciente 11, a dose absorvida pelo tumor por [$^{177}$Lu]SB3 não é suficiente para a sua erradicação, o que demonstra a importância da dosimetria pré-tratamento.

**Palavras-chave:** Antagonista de recetores GRP; PET/CT; Teranóstica; Dosimetria; Farmacocinética; Modelos Compartimentais; Cancro da Próstata

# Contents

# List of Figures

# List of Tables

# List of Abbreviations and Acronyms

| | |
|---|---|
| **1TCM** | One-tissue compartment model |
| **2TCM** | Two-tissue compartment model |
| $^{18}$**F** | Fluorine-18 |
| $^{68}$**Ga** | Gallium-68 |
| $^{68}$**Ge** | Germanium-68 |
| $^{68}$**Zn** | Zinc-68 |
| $^{137}$**Cs** | Cesium-137 |
| $^{176}$**Lu** | Lutetium-176 |
| $^{176}$**Yb** | Ytterbium-176 |
| $^{177}$**Lu** | Lutetium-177 |
| $^{177m}$**Lu** | Metastable state of Lutetium-177 |
| **ACD** | Annihilation Coincidence Detection |
| **AIF** | Arterial Input Function |
| **BGO** | Bismuth Germanate |
| **Bq** | Becquerel |
| **BW** | Body Weight |
| **cpm** | Counts per minute |
| **cps** | Counts per second |
| **CT** | Computed Tomography |
| **EANM** | European Association of Nuclear Medicine |
| **EBRT** | External Beam Radiotherapy |
| **EC** | Electron Capture |
| **ED** | Effective Dose |
| **Erasmus MC** | Erasmus Medical Center |
| **FOV** | Field of View |
| **GRPR** | Gastrin-releasing Peptide Receptor |
| **Gy** | Gray |
| **HCl** | Hydrochloric Acid |
| **IA** | Injected Activity |
| **ICRP** | International Commission on Radiological Protection |
| **IDIF** | Image Derived Input Function |
| **IPO-Porto** | Instituto Português de Oncologia Francisco Gentil, EPE do Porto |
| **IV** | Intravenous (administration) |
| **LOR** | Line of response |
| **LSO** | Lutetium Oxyorthosilicate |
| **mbp** | Minutes (per) bed position |
| **MCA** | Multichannel Analyzer |

| | |
|---|---|
| **MIRD** | (Committee on) Medical Internal Radiation Dose |
| **MRI** | Magnetic Resonance Imaging |
| **NET** | Neuroendocrine Tumour |
| **OSEM** | Ordered Subset Expectation Maximization (algorithm) |
| **PET** | Positron Emission Tomography |
| **PHA** | Pulse-Height Analyzer |
| **PM** | Photomultiplier (tubes) |
| **PRRT** | Peptide Receptor Radionuclide Therapy |
| **PSA** | Prostate-specific Antigen |
| **PSMA** | Prostate-specific Membrane Antigen |
| **PTX** | Patient X, where X is the number of the patient |
| **PVE** | Partial Volume Effect |
| **RC** | Recovery Coefficient |
| **ROI** | Region Of Interest |
| **SB3** | Sarabesin 3 |
| **SCA** | Single Channel Analyzer |
| **SE** | Standard Error |
| **SPECT** | Single-photon Emission Computed Tomography |
| **SSA** | Somatostatin Analogue |
| **SSTR** | Somatostatin Receptor |
| **SUV** | Standardized Uptake Value |
| **TAC** | Time Activity Curve |
| **TIAC** | Time-integrated Activity Coefficient, also known as Residence Time |
| **VOI** | Volume Of Interest |

# 1 Introduction

The concept of personalized medicine has been discussed in the last few years as a need to improve therapy effectiveness and reduce side effects for the patients. Therefore, an effort has been made among the scientific community to develop patient selection methods for some treatments that tend to be aggressive and usually represent high costs for the medical institutions. In Nuclear Medicine, a theranostic approach was introduced relying on diagnostic imaging and therapy using the same or very identical molecules, which are labelled with distinct radioisotopes or administrated in a different amount. The idea is to visualize potential targets at first and then estimate the therapy response and eventual toxicity.

Theranostics has proven to be a powerful strategy in cancer treatment, especially when dealing with neuroendocrine tumours (NETs). Well-differentiated NETs overexpress somatostatin receptors (SSTRs), whose imaging is crucial in staging, treatment planning and follow-up of the disease. Diagnosis is accomplished with a PET/CT scan using a somatostatin analogue (SSA) tracer labelled with $^{68}$Ga: DOTA-TATE, DOTA-TOC or DOTA-NOC. Patients with advanced metastatic neuroendocrine neoplasia are typical candidates for peptide receptor radionuclide therapy (PRRT) if good tumour uptake is detected in the PET images. In a therapeutic context, it is possible to label DOTA-TATE or DOTA-TOC with the $\beta$-emitting radionuclides $^{90}$Y or $^{177}$Lu. Since the kidneys and red bone marrow are the most limiting organs for these therapies, $^{177}$Lu is generally preferred over $^{90}$Y for being less nephrotoxic and hematotoxic due to its smaller range and lower energy, allowing the PRRT to be performed in several cycles.[1] In addition, $^{177}$Lu is not a pure beta emitter like $^{90}$Y, since it releases electrons and gamma photons during decay, enabling treatment control through imaging techniques.

Recently, the potential of the theranostic principle has been investigated in prostate cancer, which is globally the most common oncologic condition in men. $^{68}$Ga PET/CT imaging with prostate-specific membrane antigen (PSMA) ligands has been established as one of the best methods to detect prostate cancer, especially when biochemical recurrence of the disease is verified after radical prostatectomy or radiotherapy procedures, since PSMA is highly expressed in poorly differentiated metastatic tumours. [2] Furthermore, PSMA probes are also known for an outstanding job in diagnosing androgen-dependent tumours with bone metastasis but have shown lower sensitivity in identifying primary carcinomas. [3] This insight led us to conclude that radionuclide therapy using PSMA inhibitors labelled with $^{177}$Lu might be feasible in late stages of prostate cancer. Many studies have been performed around this topic, which is currently undergoing clinical validation. One of the major concerns is the absorbed dose in normal organs like the kidneys and salivary glands, due to tracer excretion and significant presence of PSMA expression, respectively. [4]

At the present time, detection of prostate cancer involves, at first instance, the mea-

surement of the level of prostate-specific antigen (PSA) in blood. High levels of this protein are often associated to prostate carcinoma and the application of imaging techniques like MRI, CT and ultrasound may posteriorly lead to an accurate diagnosis. However, these imaging procedures are usually associated with lack of diagnostic specificity. In these cases, taking biopsies of the prostate is needed to confirm the presence of the disease, in spite of being a very invasive and unpleasant method for the patients.

In previous studies, it was reported that primary and well-differentiated prostate cancer lesions also show high density expression of gastrin-releasing peptide receptors (GRPRs) and 50% chance of GRPR expression in androgen-dependent bone metastasis. Therefore, targeting these receptors for tumour imaging was proposed as an alternative for diagnosing primary and/or advanced disease stages with higher specificity and sensitivity.

Sarabesin 3 (SB3) is a bombesin analogue and a GRPR antagonist. In opposition to receptor agonists, it targets the GRPR without being internalized into the cancer cells, preventing pharmacological effects after receptor binding and ensuring good drug tolerance after IV administration to the patients. It is expected that [$^{68}$Ga]SB3 imaging will provide a better diagnosis of prostate cancer in primary stages of the disease, becoming a complement of [$^{68}$Ga]PSMA, whose strength is undeniable in advanced cases. There is also a possibility to label SB3 with $^{177}$Lu for therapy applications, which immediately suggests a theranostic approach. [5]

In the present work, a clinical study involving 11 patients with prostate cancer was performed in order to evaluate the diagnostic potential and radiation dosimetry of [$^{68}$Ga]SB3, as well as the possibility of [$^{177}$Lu]SB3 administration for targeted prostate cancer therapy. Additionally, the pharmacokinetic behaviour of the imaging tracer was investigated individually using compartmental modelling techniques. The purpose was to inspect whether this approach would be suitable as a patient selection method for therapy. Finally, tumour dosimetry estimations were carried out to complement the decision process.

Apart from this introductory chapter, this dissertation features five more chapters. The second one encounters some background information on PET, well-counter systems and $^{68}$Ga imaging characteristics. The next two sections report some details about the equipment, the clinical procedure and data assessment methods employed in this study. In chapter 3, the relevant quantities in internal exposure are presented, along with the formalism of clinical dosimetry and the mathematical fundamentals of compartmental modelling. The forth chapter highlights the role of $^{177}$Lu in targeted radionuclide therapy, together with some insight on how to estimate the absorbed doses to the potential organs at risk and to the tumour from $^{68}$Ga imaging data. Chapter 5 presents the results of the research work along with the respective discussion and the last chapter exhibits the conclusions and perspectives on the future work.

The work for this dissertation was accomplished as a part of the master's programme in Medical Physics provided by the Science Faculty of the University of Porto (FCUP), in

particular as a collaboration between the Portuguese Institute of Oncology (IPO-Porto) and the Erasmus Medical Center in Rotterdam, the Netherlands. The internship lasted 5 months, between February and June 2019, and was supported by the Erasmus+ programme.

# 2 Image acquisition and patient data assessement

## 2.1 Positron emission tomography

Positron Emission Tomography (PET) is one of the tomographic imaging methods applied in Nuclear Medicine. It relies on the administration of radiopharmaceuticals, whose structure is composed by a positron emitting radioisotope bound to a specific tracer. As soon as the tracer targets the respective receptor, the radioisotope starts emitting positrons by $\beta^+$ decay that will interact with electrons present in body tissue, originating photons. For each positron that results from the decay, two 511-keV photons are released in opposite directions in a process designated by pair annihilation. The detection in coincidence of these two photons allows image reconstruction of the activity distribution in the targeted organs, giving access to their physiological information (figure 2.1).

In the acquisition process, the multiple detectors are organized in an array of multiple rings around the organ of interest. Therefore, data is collected in a 360º angle around the patient body through a process designated as Annihilation Coincidence Detection. ACD determines that two photons are in coincidence when they fall within a specified coincidence timing window, usually set up for 6 to 12 nanoseconds. As a result, each photon pair is detected without using absorptive collimators in a mechanism denominated by electronic collimation. When a coincidence event is identified, it is created a line of response (LOR) between the two detectors that encounters the location of the annihilation event. The simultaneous acquisition of multiple LORs allows the performance of a 3D reconstruction and, consequently, the access to the activity distribution of the patient slice being scanned. PET and Computed Tomography (CT) are usually combined in the same device, as CT information is crucial to provide anatomical reference and attenuation correction in the PET images.

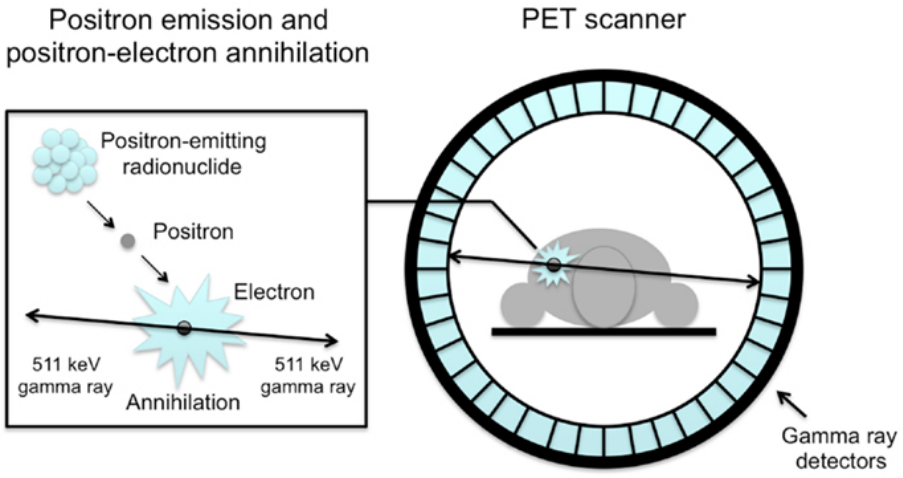


Figure 2.1: Representation of the PET principle.

PET detectors are typically composed of LSO or BGO scintillation crystals, since these materials are not hygroscopic and have high stopping power, i.e., high density and linear attenuation coefficient. Due to their scintillation properties, when gamma or x-rays interact with them via photoelectric, Compton and/or pair production processes, the crystal's molecules are excited to higher states and return to their ground states after the characteristic scintillation decay time of the crystal and emit light photons. These light photons are converted into electronic pulses and amplified by the adjacent photomultiplier (PM) tubes. Subsequently, the Pulse Height Analyzer (PHA) selects the pulses whose amplitude coincides with the desired energy and window settings. The data is then stored in the form of a sinogram where each LOR information is plotted in (r,$\phi$) coordinates. For a specific projection, adjacent detector pairs form parallel LORs for the same angle of orientation. In short, a sinogram will represent a single slice of data for a transverse FOV collected from a single ring of the PET device. To perform a whole-body scan of a patient, there is a computed-monitored bedtable that moves long the axis of the detector ring.

After reconstruction, PET images can be analysed qualitatively and quantitatively. The first relies on the observation of the radiopharmaceutical distribution and identification of uptake regions within the human body, whereas the other encounters the determination of radiotracer concentration based on the Standardized Uptake Value (SUV). This quantification is performed in static images, whose analysis is the basis to accomplish dosimetric studies.

The SUV is defined as the radiopharmaceutical concentration in tissue ($c_t$) normalized by the injected activity (IA) and patient body weight (BW), as presented in the following formula:

$$SUV\ (g/ml) = \frac{c_t\ (MBq/mL)}{IA\ (MBq)/BW\ (g)} \tag{1}$$

This parameter allows activity quantification in a region of interest (ROI) independently of the administered activity and patient body weight. However, a correction for the physical decay of the radionuclide should be applied to assess the total amount of activity concentration in the tissue.

In equation (1), SUV can assume different forms depending on how the ROI is analysed, such as $SUV_{max}$ and $SUV_{mean}$. The former designation reports to the highest pixel value within the drawn ROI, whereas the latter corresponds to a mean pixel value. For dosimetry purposes, the $SUV_{mean}$ gives the most accurate estimation for the organ uptake, as long as the ROI is faithfully placed inside the tissue region and surrounding the hottest pixel and the organ uptake is homogeneous.

## 2.2 Gallium-68 imaging characteristics

Although fluorine-18 ($^{18}$F) is the standard PET radioisotope, gallium-68 is currently becoming more and more attractive among this field, mostly in research applications. In practice, the first aspect that stands out is its commercial access from a germanium-68 ($^{68}$Ge) generator and consequent dispensable presence of a cyclotron nearby. The half-life of $^{68}$Ge is 270.95 days but a single clinical $^{68}$Ge/$^{68}$Ga generator can only be used during 9 to 10 months, due to quality standards for sterility and collumn decline with acid eluates. The equilibrium between the two radioisotopes is quickly established after $^{68}$Ga elution with hydrochloric acid (HCl) to prepare several radiopharmaceuticals. It also allows to collect information about different physiologic functions, which tend to be more complex to image with $^{18}$F such as overexpression of somatostatin receptors and PSMA, which are characteristic of neuroendocrine and prostatic tumours, respectively. A simplified scheme including the decays of $^{68}$Ge and $^{68}$Ga is presented in figure 2.2.

From the physical point of view, there are some properties of $^{68}$Ga that are linked with poorer image quality with respect to $^{18}$F. First, $^{68}$Ga disintegrates faster than $^{18}$F (half-life of 67.71 min against 109.77 min), meaning that the time between injection and imaging plays a significant role in the radioactivity flow from the blood to the organs. At the same time, $^{68}$Ga manifests a lower positron yield (88.88% in opposition to 96.86% for $^{18}$F), which is translated in a lower detection sensitivity. Unlike $^{18}$F, $^{68}$Ga releases during decay single photons with energies in the interval of 350-700 keV due to transitions from excited states to the ground state of $^{68}$Zn with small probability, and also some scattered photons, which contribute to the increase of image noise (figure 2.3). However, the main gamma emission of $^{68}$Ga has an energy of 1077 keV, which falls outside the window of the PHA included in the PET system and does not affect the image quality.

On top of that, there is quite a difference in the positron energy spectrum during the decay of both radioisotopes. Higher end point of positron energy is verified for $^{68}$Ga in relation to $^{18}$F (figure 2.4 (a)), which culminates in a higher distance between the annihilation site and the position where the positron was emitted and, consequently, has

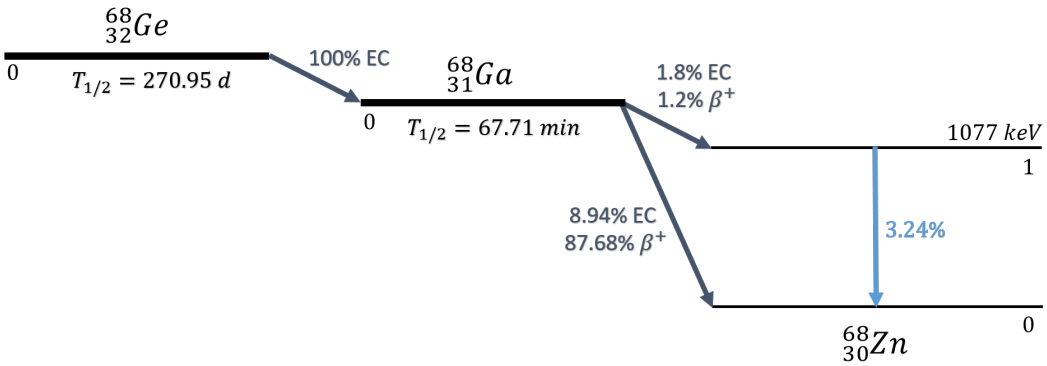


Figure 2.2: Simplified decay scheme of $^{68}$Ge and $^{68}$Ga. [6]

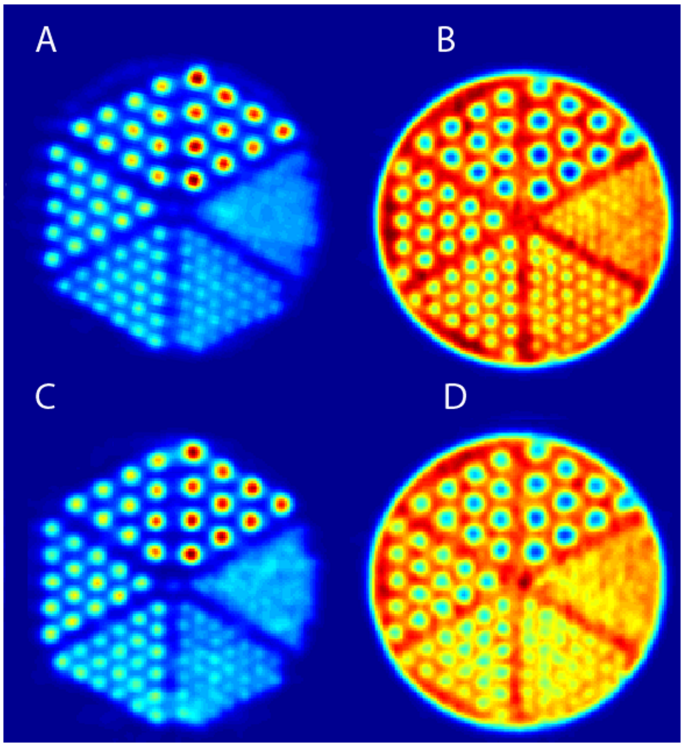


Figure 2.3: Comparison between image quality in reconstructed images of the Jaszczak SPECT/PET spatial resolution phantom with $^{18}$F (A and B) and $^{68}$Ga (C and D). Images recorded with the clinical system Siemens Biograph 64. OSEM was employed in reconstruction. [7]

a negative impact in spatial resolution and originates partial volume effects (PVEs). In general, the potential of recovering the true activity in $^{68}$Ga images is lower, meaning that the measured activity is substantially underestimated. PVE is particularly relevant for small size spheres in clinical PET, as shown in figure 2.4 (b). The recovery coefficients (RCs) depend also on the PET scanner and are pre-calculated using phantoms with similar characteristics (shape and size) as the volume of interest. A RC is defined as the ratio between the activity measured in the PET image and the true activity in the phantom. Therefore, RCs are helpful to correct the SUV or activity concentration in a certain object without changing the image.

Surprisingly, all these drawbacks of $^{68}$Ga imaging are somehow balanced by the high specificity and lower background activity of the uptake of $^{68}$Ga labelled agents with respect to $^{18}$F labelled FDG, leading to a higher image contrast (figure 2.5).

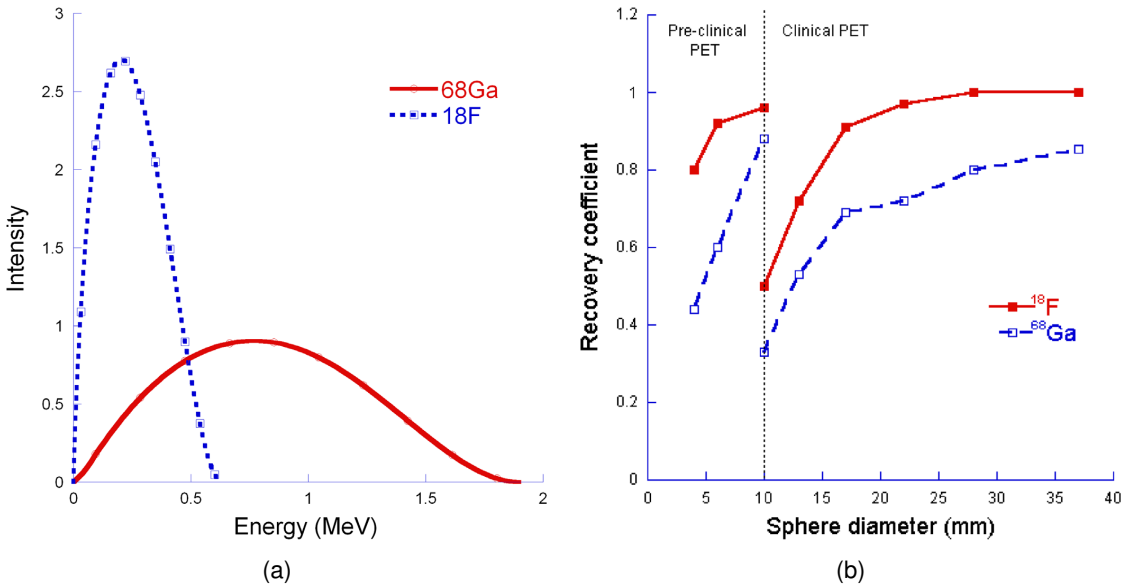


Figure 2.4: (a) Energy distribution of the positron emission of $^{68}$Ga and $^{18}$F; (b) Pre-calculated recovery coefficients as a function of object size for $^{18}$F and $^{68}$Ga in a clinical PET scanner (Siemens Biograph 64) and respective pre-clinical scanner.[7]

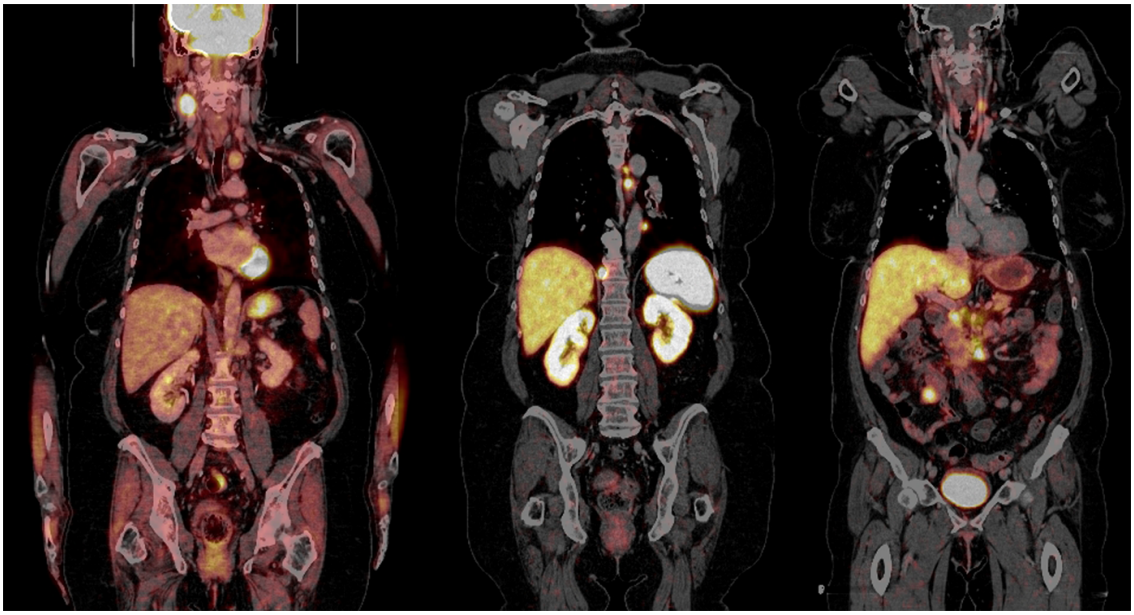

Figure 2.5: Clinical FDG and [$^{68}$Ga]DOTATOC PET/CT images of a patient with an unknown primary tumour. The image on the left shows a FDG PET/CT coronal view with low specific uptake in the entire body including the lymph node metastasis in head and neck. Other lymph node metastasis were found in the CT images but with low FDG uptake. The primary tumour was not identified. Central and right scans show a coronal section of the same patient imaged with [$^{68}$Ga]DOTATOC one month later. Central figure displays several lymph node metastasis with intense DOTATOC uptake, corresponding to the anatomical changes observed in the previous FDG PET/CT scan. Right figure reveals a clearly defined and intense lesion in the distal ileum, corresponding to the location of the primary tumour, along with multiple abdominal metastasis.[7]

## 2.3 Well-counter system

Radiation counting systems have multiple applications in Nuclear Medicine, not only in measuring radioactivity in tissue, blood and urine samples, but also in monitoring radioactive assays in radiobiology and radiochemistry. They can be composed of a single unit controlled manually or encountered in a computer-assisted system capable of measuring multiple samples sequentially. One of the most efficient systems for counting gamma radiation is a well counter, commonly designated as gamma counter, with a scintillation NaI(Tl) crystal in its constitution (figure 2.6). The crystal features a hole or well in one end where a test tube containing the sample is placed. Well counter systems are usually shielded with lead to reduce the amount of background counts. Moreover, the crystal emits light that is converted in an electronic signal by an adjacent PM tube. Thus, the working principle is identical to the one described previously for a PET ring of detectors. However, gamma counters tend to be less efficient than PET detectors because of reflection and scattering of light in the walls of the well inside the scintillation crystal. Among its components, there is also a high voltage supply, a preamplifier, an amplifier, single-channel analysers (SCAs) or a multichannel analyser (MCA) to perform PHA, a digital or analogue scaler-timer and a rate meter that converts the pulses in counts per minute (cpm) or counts per second (cps).

Gamma counters require periodical calibration to ensure that the PHA discriminators match directly the pulse height with the respective energy of the gamma energy measured. This procedure is designated by high-voltage or energy calibration and is accom-

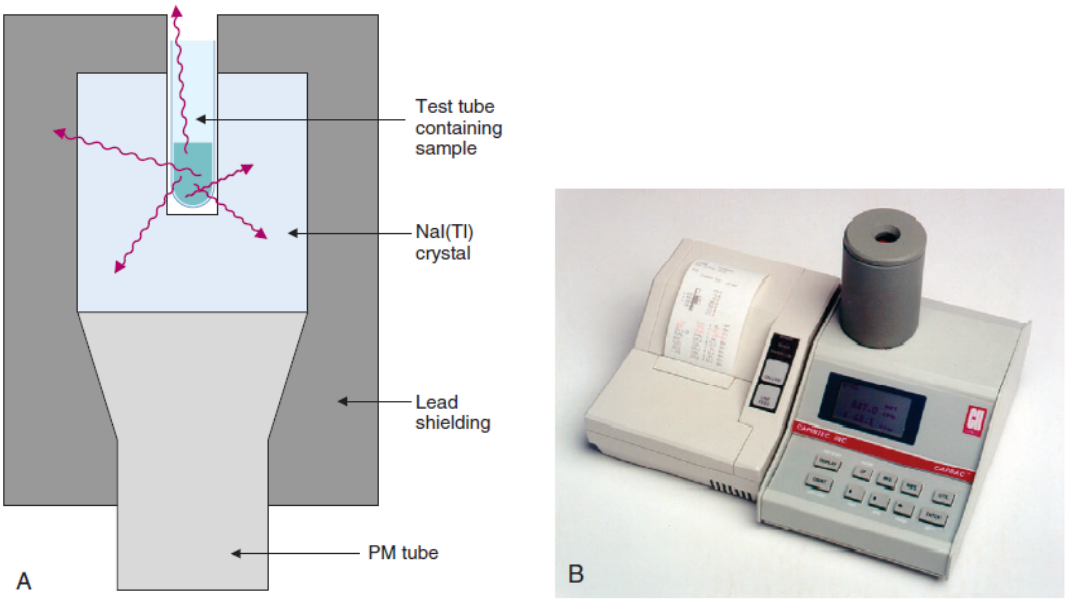


Figure 2.6: (A) Scheme of a well-counter's cross-section containing a test tube with a radioactive sample; (B) Manually operated well-counter with a digital readout and a printer (*Capitec Inc., Ramsey, NJ*).[8]

plished by inserting a $^{137}$Cs source in the well. $^{137}$Cs has a characteristic emission at 662 keV. Therefore, the lower and upper limits of the PHA are established at 640 and 684 divisions, respectively, so that the centre of the photopeak would fall at 622 divisions which is associated with the 662-keV gamma photons. The calibration process involves calibration of the count rate against a known activity, preferrably a standard activity, compared to some primary standard provided by a metrology institute.

In the interest of quantifying the absolute activity of a radioactive sample, it is important to evaluate the detection efficiency of the gamma counter for the desired gamma energy using a standard radioactive sample of known activity. The efficiency of the photopeak is given by the ratio between the count rate of the standard radioactive source obtained with the adequate PHA configuration and the disintegration rate associated to the known activity of that standard source and should be estimated for each photon energy, so that the efficiency correction could be applied to the count rates of sample with unknown radioactivity.

A given radioactive sample can release multiple gamma rays due to the presence of single or multiple radionuclides, which yields a more complex energy spectrum, since there is superposition of the multiple photopeaks, as well as formation of spillover or crosstalk contributions from Compton interactions of the high-energy photons with the lower-energy photopeaks. As a result, corrections in the energy distribution should also be applied regarding this type of phenomena.

Sample volume is also a factor that affects the counter efficiency. The bigger the sample volume with a given activity, the lower is the detector efficiency, since a larger number of photons escape from the well without interacting with the crystal. In general, detection efficiency of a gamma counter decreases when the photon energy is increased and/or detector size is reduced. Maximum detection efficiency for a given volume, activity and detector size is achieved when the sample is placed in the center of the well.

## 2.4 Equipment

The PET/CT scanner used in this clinical study was the Siemens Biograph mCT (*Siemens, Erlangen, Germany*) shown in figure 2.7, whose camera is calibrated according to the EARL protocol integrated in the european guidelines. [2] The encountered software version is the syngo MI.PET/CT 2012A. PET detectors are distributed in 4 rings with 48 detector blocks in each one. Each detector ring has a diameter of 84.2 cm. LSO crystals with size 4x4x20 mm are arranged in a 13x13 array coupled to a 2x2 PM tube array in each detector block. This configuration provides an axial PET field of view (FOV) of 22.1 cm and a transaxial FOV of 70 cm. The coincidence time window is 4.1 ns and the device offers time-of-flight performance that results in a system time resolution of 540 ps. The energy window is set up in the range of 435-659 keV. An integrated 64 or 128-slice CT is used for attenuation correction of PET data. Tube voltage options of 70, 80, 100, 120 and 140 kV are offered for CT acquisition. Lastly, it has a tunnel length of 136 cm and the table supports a maximum weight of 227 kg.[9]


Figure 2.7: Siemens Biograph mCT PET/CT scanner (*Siemens, Erlangen, Germany*).[9]

In order to quantify the activity in blood and urine samples, it was used the Perkin Elmer WIZARD 1480 automatic gamma counter (*Perkin Elmer, Massachusetts, USA*) presented in figure 2.8.[10] This equipment includes one NaI(Tl) detector shielded with 75 mm of lead and allows the measurement of 1000 samples in 13 mm diameter tubes or 270 samples in 28 mm tubes at the same time. The placement of the samples inside the well is assisted by an unique arm. According to the manufacturer, it is ideal to perform

measurements of high energy gamma emitters and low activity samples. Moreover, this device provides a high resolution MCA with 1024 channels and performes automatic corrections for the background counts and efficiency.

Figure 2.8: Perkin Elmer WIZARD 1480 automatic gamma counter (*Perkin Elmer, Massachusetts, USA*).[10]

## 2.5 Clinical procedure and data assessment

The PET/CT acquisition study protocol for [$^{68}$Ga]SB3 uptake in early stage prostate cancer patients consisted in the following proceedings:

1. dynamic list mode acquisition for 20 minutes from immediately before injection;
2. acquisition of single bed static PET images of the pelvic area at 30 and 45 minutes post injection, 6 minutes per bed position (mbp);
3. acquisition of single bed static images of upper abdomen at 36 and 51 minutes (6 mbp);
4. acquisition of whole-body images (from crown of head to lower thigh) at 60 and 120 minutes using 7 bed positions (4 mbp except for pelvic area, which were 6 mpb);
5. acquisition of single bed static images of the pelvic area at 150 and 210 minutes (12 mbp);
6. acquisition of single bed static PET images of upper abdomen at 170 minutes (12 mbp).

All PET acquisitions were preceded by a low dose CT scan using 120 kVp and 40 ref mAs for the static PET scans or 120kVp and 20 ref mAs for the whole-body PET scans. The administrated activities of [$^{68}$Ga]SB3 and body weight values are presented in table 2.1 for each patient.

PET image reconstruction was performed with an ordered subset expectation maximization (OSEM) algorithm using resolution recovery, time-of-flight information, 3 iterations, 21 subsets and a 3 mm post-reconstruction Gaussian filter. Attenuation and scattering corrections were also applied during reconstruction.

| Patient number | Administered activity (MBq) | Body weight (kg) |
|---|---|---|
| 1 | 159 | 83 |
| 2 | 155 | 92 |
| 3 | 130 | 88 |
| 4 | 247 | 92 |
| 5 | 210 | 82 |
| 6 | 159 | 100 |
| 7 | 150 | 88 |
| 9 | 260 | 90 |
| 10 | 210 | 69 |
| 11 | 206 | 82 |
| 12 | 158 | 87 |

Table 2.1: Individual administered activities of [$^{68}$Ga]SB3 and patient body weights in MBq and kg, respectively.

Regarding image measurements, volumes-of-interest (VOI) were drawn on the PET/CT fusion images using *OsiriX 5.9* (Pixmeo Sàrl, Bernex, Switzerland). Quantification of uptake, was expressed by the SUV and corrected for injected dose, body weight and radioactive decay.

It should be noted that the acquisition procedure mentioned in this section took place in 2017. Therefore, the data analysis presented in this dissertation was based in SUV measurements and blood and urine activity counts that were previously collected.

# 3 Clinical dosimetry and pharmacokinetic modelling

## 3.1 Dosimetric quantities in internal exposure

In Nuclear Medicine, it is of extreme importance the quantification of internal exposure from radionuclides, especially in therapeutic procedures. In diagnostic applications, sometimes the high doses are justified if they lead to a well funded diagnosis. Either way, the fundamental dose quantity is the mean organ or tissue absorbed dose $D_T$, which is defined as the ratio between the total energy imparted by ionising radiation $\epsilon_T$ to organ or tissue T and its mass $m_T$, as showed in equation (2). It is expressed in joules per kilogram (J/kg) in SI units, which is equivalent to gray (Gy).

$$D_T = \frac{\epsilon_T}{m_T} \tag{2}$$

However, it is common knowledge in radiobiology that different types of ionising radiation cause different degrees of damage in a given organ for the same delivered dose. For instance, alpha particles and neutrons are more harmful for a certain tissue, when exposed to the same dose, than gamma rays or electrons , due to their higher capability of producing irreversible damage by dense ionisation phenomena. In order to include this evidence, a new definition of dose was introduced. The equivalent dose $H_T$ is the multiplication of the organ absorbed dose by a radiation weighting factor $w_R$ that considers the biological effect of the type of radiation delivered to that organ, as displayed in equation (3). Thus, $D_{T,R}$ becomes the mean absorbed dose in an organ or tissue by type $R$ radiation.

$$H_T = w_R D_{T,R} \tag{3}$$

Equivalent dose is also expressed in joule per kilogram (J/kg), but in this case it corresponds to a sievert (Sv). The values of weighting factors $w_R$ for each type of radiation are shown in table 3.1 according to the ICRP Publication 60 but they were posteriourly updated on the ICRP Publication 103 (table 3.2). All values correspond to radiation either incident in the body or emitted internaly from radionuclides. The total equivalent dose in a tissue is given by the sum of the equivalent doses for each type radiation present in an exposure procedure.

| **Radiation type** | **Radiation weighting factor** $w_R$ |
|---|---|
| Photons, electrons and muons | 1 |
| Protons, other than recoil protons<br>Energy $>$ 2 MeV | 5 |
| Alpha particles, fission fragments<br>and heavy ions | 20 |
| Neutrons | |
| Energy $<$ 10 keV | 5 |
| 10 keV to 100 keV | 10 |
| $>$ 100 keV to 2 MeV | 20 |
| $>$ 2 MeV to 20 MeV | 10 |
| $>$ 20 MeV | 5 |

Table 3.1: Weighting factors $w_R$ for each type of radiation according to ICRP Publication 60. [11]

| **Radiation type** | **Radiation weighting factor** $w_R$ |
|---|---|
| Photons, electrons and muons | 1 |
| Protons and charged pions | 2 |
| Alpha particles, fission fragments<br>and heavy ions | 20 |
| Neutrons | |
| $E_n <$ 1 MeV | $2.5 + 18.2e^{-[ln(E_n)]^2/6}$ |
| 1 MeV $\leq E_n \leq$ 50 MeV | $5.0 + 17.0e^{-[ln(2E_n)]^2/6}$ |
| $E_n >$ 50 MeV | $2.5 + 3.25e^{-[ln(0.04E_n)]^2/6}$ |

Table 3.2: Weighting factors $w_R$ for each type of radiation according to ICRP Publication 103. For neutrons, the factor depends on the their energy $E_n$.[12]

The effects of radiation exposure at a cellular level can be split into two groups. The first one incorporates deterministic effects, which reflect themselves in malfunction of cells after exposure to high doses of radiation, and the second one includes stochastic effects, which are related to cancer and hereditary disorders induced by radiation exposure at low doses. Stochastic effects have a certain probability of being induced depending on the type of organ or tissue being irradiated. To account this factor, a quantity denominated as effective dose E was presented in ICRP Publication 60 as a weighted sum of the tissue equivalent doses

$$E = \sum_T w_T H_T \tag{4}$$

where $w_T$ is the tissue weighting factor for tissue T. The $w_T$ factors represent the contribution of each tissue of the human body, in which there is a probability of inducing stochastic effects, to the overall radiation dose. The SI unit for effective dose is joule per kilogram (J/kg), also denominated as sievert (Sv) like for the equivalent dose.

In practice, it is not possible to measure equivalent dose or effective dose. The dose coefficients relative to the internal exposure from radionuclides are estimated using biokinetic models, reference physiological data or computational phantoms. At the present time, computational phantoms of the adult Reference Male and adult Reference Female are employed, whose organs are designed to match the organ masses defined for a reference adult in ICRP Publication 89. [13] Significant anatomical differences between male and female adults led to the definition of a new effective dose, in which tissue weighting factors are sex- and age-averaged for all organs and tissues, also involving male and female breast, testis and ovaries. Thus, according to ICRP Publication 103, the effective dose is determined from the equivalent doses of each organ or tissue T of the Reference Male ($H_M^T$) and of the Reference Female ($H_F^T$) as in following formula

$$E = \sum_T w_T \left[ \frac{H_M^T + H_F^T}{2} \right] \tag{5}$$

Recent and old tissue weighting factors $w_T$ are displayed in tables 3.3 and 3.4. In the recent table, the remainder includes 13 different tissues: adrenals, extrathoracic (ET) region, gall bladder, heart, kidneys, lymphatic nodes, muscle, oral mucosa, pancreas, prostate (for male), small intestine, spleen, thymus, uterus/cervix (for female).Therefore, the equivalent doses to remainder tissues of the Reference Male ($H_{rmd}^M$) and Reference Female ($H_{rmd}^F$) are given by

$$H_{rmd}^M = \frac{1}{13} \sum_T^{13} H_M^T \qquad H_{rmd}^F = \frac{1}{13} \sum_T^{13} H_F^T \tag{6}$$

| **Tissue** | **Tissue weighting factors** $w_T$ |
|---|---|
| Bone surfaces | 0.01 |
| Bladder | 0.05 |
| Breast | 0.05 |
| Colon | 0.12 |
| Gonads | 0.20 |
| Liver | 0.05 |
| Lungs | 0.12 |
| Oesophagus | 0.05 |
| Red bone marrow | 0.12 |
| Skin | 0.01 |
| Stomach | 0.12 |
| Thyroid | 0.05 |
| Remainder | 0.05 |
| **TOTAL** | 1.00 |

Table 3.3: Tissue weighting factors $w_T$ according to ICRP Publication 60. [11]

| **Tissue** | $w_T$ | $\sum w_T$ |
|---|---|---|
| Red bone marrow, Colon, Lung, Stomach, Breast and Remainder | 0.12 | 0.72 |
| Gonads | 0.08 | 0.08 |
| Bladder, Oesophagus, Liver, Thyroid | 0.04 | 0.16 |
| Bone surface, Brain, Salivary Glands, Skin | 0.01 | 0.04 |
| **TOTAL** | | 1.00 |

Table 3.4: Tissue weighting factors $w_T$ according to ICRP Publication 103. [12]

Figure 3.1 explains schematically how to obtain the sex-averaged effective dose, commonly designated as effective dose 103. This quantity only takes into account the exposure conditions and the tissue weighting factors are mean values estimated from many individuals of both sexes.

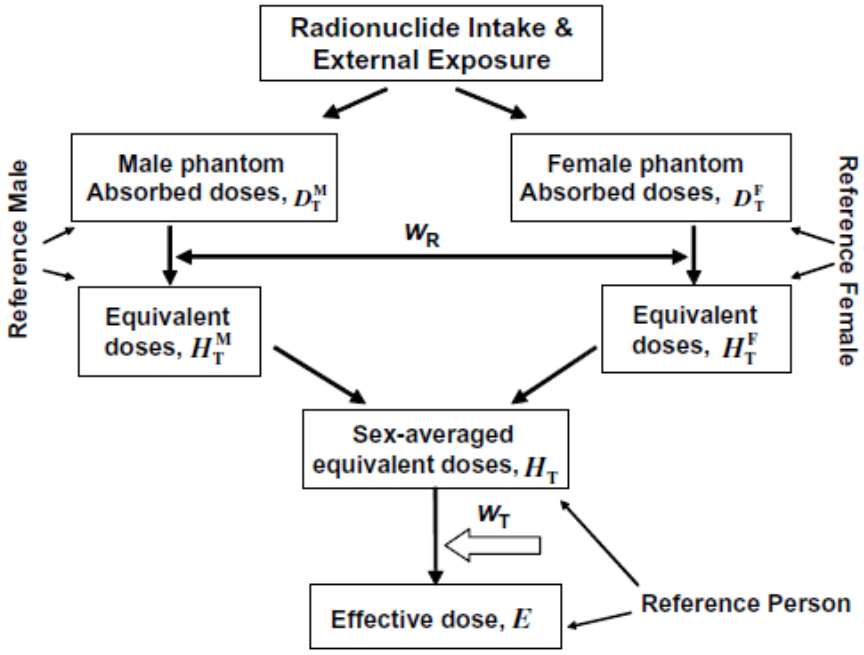


Figure 3.1: Calculation steps to obtain the effective dose 103.[12]

## 3.2 Dosimetry formulation

Part of the Society of Nuclear Medicine, the Committee on Medical Internal Radiation Dose (MIRD) made an effort to unify the methods and notation employed in internal dosimetry calculations along with the International Commission on Radiological Protection (ICRP), which culminated in the publication of the MIRD Pamplet No. 21 [14, 15]. According to this latest formalism, the absorbed dose $D$ to a target region $r_T$ due to the activity in a source region $r_S$ is obtained by the following relation between the time-integrated activity $\tilde{\mathrm{A}}$ and the S-value

$$D(r_T) = \tilde{\mathrm{A}}(r_S) \cdot S(r_T \rightarrow r_S) \tag{7}$$

Absorbed dose values are expressed in joule per kilogram (J/kg) in SI units, which commonly known as gray (Gy).

The S-value represents the absorbed dose rate per unit activity in $Gy \cdot (Bq \cdot s)^{-1}$ and its definition is presented in equation (8). It depends not only on the energy emitted by the radionuclide ($E$) and the probability $Y$ of that emission, but also on the absorbed fraction $\phi$ and the mass of the target region $M(r_T)$. The absorbed fraction $\phi$ is denoted as the fraction of energy emitted by the source region that is absorbed in the target region, i.e., it is a value between 0 and 1. Many factors influence this later quantity such as the shape, size and mass of the source and target regions, as well as the distance and type of material between the source and the target regions, and also the type of radiation emitted by the source and its energy. Therefore, all these aspects also have an impact on the S-value.

$$S = \frac{EY\phi}{M(r_T)} \tag{8}$$

S-values for a given radionuclide and source-target arrangement are generated from Monte Carlo simulations using anatomical phantoms.

The time-integrated activity $\tilde{\mathrm{A}}(r_S)$ indicates the number of desintegrations that occur in a specific source region in $Bq \cdot s$. This latter quantity is usually calculated as the area under the time-activity curve on the source region after the injection of the radiotracer, i.e., can be calculated as the integration of the activity of the source region $A(r_S, t)$ over a period $T_D$

$$\tilde{\mathrm{A}}(r_S, T_D) = \int_0^{T_D} A(r_S, t)dt \tag{9}$$

The integration period $T_D$ is often chosen from the time of injection of the radiotracer ($t = 0$) until infinity ($t = \infty$), since the radionuclides used in nuclear medicine procedures have relatively short physical half-lives.

The time-integrated acitivity coefficient of the source region $\tilde{a}(r_S)$ (TIAC), which is a new designation for the residence time [14], is also an important quantity on dosimetry studies. It is expressed in units of time and defined by

$$\tilde{a}(r_S) = \frac{\tilde{A}(r_S)}{A_0} \tag{10}$$

where $A_0$ is the radiopharmaceutical administered activity. It is interpreted as an average time that the radioactivity spends in a source region.

The activity in the target region as a function of time $A(r_S, t)$ is usually characterised by a sum of exponential functions as presented in equation (11). For all $j$ exponentials, $A_j$ denotes the respective initial activity, $\lambda_p$ the physical decay constant of the radioisotope, $\lambda_j$ the biological decay constant and $t$ the time after the injection of the radiotracer.

$$A(r_S, t) = \sum_j A_j \cdot e^{-t(\lambda_p + \lambda_j)} \tag{11}$$

Each decay constant $\lambda$ is related with its respective half-life $T_{1/2}$ as presented in equation (12). The physical half-life $T_{1/2,p}$ and the biological half-life $T_{1/2,j}$ can be incoporated in an effective half-life $T_{1/2,eff}$ as in equation (13), which is always shorter than the physical and biological half-lives apart.

$$\lambda = \frac{ln(2)}{T_{1/2}} \tag{12}$$

$$\frac{1}{T_{1/2,eff}} = \frac{1}{T_{1/2,p}} + \frac{1}{T_{1/2,j}} \tag{13}$$

Combining equations (9) and (11), it is clear that the time-integrated activity $\tilde{A}(r_S)$ when the activity of a source region $A(r_S, t)$ is described by a single exponential curve is

$$\tilde{A}(r_S) = \int_0^\infty A(r_S, 0) \cdot e^{-t(\lambda_p + \lambda_j)} = \frac{A(r_S, 0)}{\lambda_p + \lambda_j} \tag{14}$$

Other integration methods can be employed like trapezoidal or Riemann integration, depending on how well the time-acitivity curve is fitted. A representation of the three integration methods is shown in figure 3.2. In order to achieve a reasonable fitting, at least three data points per exponential phase are required and the data should be recorded along two to three effective half-lives of the radionuclide in question (at minimum).

Finally, according to the bladder model elaborated in the MIRD Pamphlet No. 14 [16], it is possible to estimate the time-integrated activity coefficient $\tilde{a}(r_S)$ of the urinary bladder

wall due to the radioactivity clearance through the urine as presented in the following equation

$$\tilde{\mathrm{a}}(r_S) = \sum_j \alpha_j \left[ \frac{1 - e^{\lambda_p T_\nu}}{\lambda_p} - \frac{1 - e^{(\lambda_p + \lambda_j) T_\nu}}{\lambda_p + \lambda_j} \right] \times \left[ \frac{1}{1 - e^{(\lambda_p + \lambda_j) T_\nu}} \right] \tag{15}$$

where $\alpha_j$ stands for the biologic coefficients representing the fraction of the administered activity entering the bladder for the $j^{th}$ component, $\lambda_j$ is the biologic rate constant for entry of the $j^{th}$ component into the bladder and $T_\nu$ is the voiding time interval.

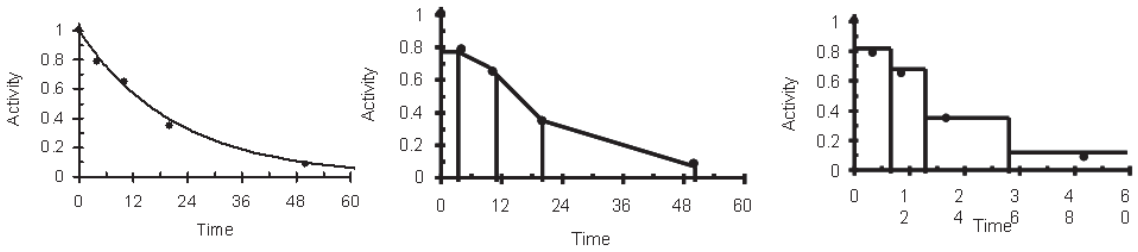


Figure 3.2: Different ways of calculation the time-integrated activity: (a) fitting the curve with an exponential function; (b) trapezoidal integration; (c) Riemann integration.[15]

## 3.3 Compartmental modelling

Compartmental modelling is a mathematical strategy to examine dynamic PET data that allows the characterization of the radiopharmaceutical's kinetics and prediction of its interaction with the different tissues. This concept relies on separating the different physiological states of the tracer into different compartments that interact with each other through transfer rates. The first compartment of every model represents the arterial blood and the number of compartments added to the model depends on the chemical and biological properties of the radiotracer.[17] The simplest model encounters a one-tissue compartment (figure 3.3) and the exchange between the two compartments is characterized by two rate constants $K_1$ (in $ml \cdot g^{-1} \cdot min^{-1}$) and $k_2$ (in $min^{-1}$), which describe the uptake and clearance of the pharmacon.

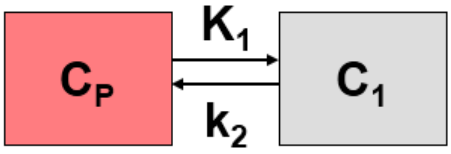


Figure 3.3: One-tissue compartment model.[18]

The concentration of the tracer in the tissue ($C_1$) can be assessed by solving the following differential equation

$$\frac{dC_1(t)}{dt} = K_1 C_P(t) - k_2 C_1(t) \tag{16}$$

where $C_P$ is the concentration of the tracer in the arterial plasma. In this model, the concentration in the tissue represents the free and non-specific binding of the tracer, i.e., the perfusion of the tissue. The model curve is given by

$$C_{model}(t) = (1 - \nu_B) C_1(t) + \nu_B C_B(t) \tag{17}$$

where $\nu_B$ is the blood volume fraction and $C_B(t)$ the concentration of the tracer in the whole blood.

The kinetics of some radioligands matches with a two-tissue compartmental model (figure 3.4), which includes an extra compartment that represents the specific binding of the tracer and whose concentration is $C_2$. The exchange between tissue compartments is expressed by the rate constants $k_3$ and $k_4$, both in $min^{-1}$. Tissue concentrations $C_1$ and $C_2$ are associated with two differential equations (18, 19).

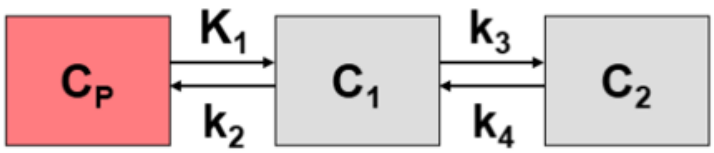


Figure 3.4: Two-tissue compartment model.[18]

$$\frac{dC_1(t)}{dt} = K_1 C_P(t) - (k_2 + k_3)C_1(t) + k_4 C_2(t) \tag{18}$$

$$\frac{dC_2(t)}{dt} = k_3 C_1(t) - k_4 C_2(t) \tag{19}$$

The model curve is given by

$$C_{model}(t) = (1 - \nu_B)(C_1(t) + C_2(t)) + \nu_B C_B(t) \tag{20}$$

Therefore, it is possible to solve the differential equations associated to the model based on the activity curves of the arterial plasma and of the tissue over time and, consequently, reach the concentrations in each compartment together with the rate constants that characterize compartment exchange. These parameters describe quantitatively the pharmacokinetics of the tracer.

It is worth noting that the equations associated to the compartmental models presented in this section are only valid when the physical decay constant of the radioisotope in question is negligible when compared to the biological decay constant of the same radioisotope in the tissue being analysed.

Biokinetic models and data of different radiopharmaceuticals have been reported in several publications of the ICRP over the years, being the ICRP Publication 128 the most recent one related to this topic. [19]

## 3.4 Software

In spite of using Microsoft Excel, Office 365 *(Microsoft, Washington, USA)* to organize the data and perform intermediate calculations, some specific software was also employed, whose characteristics are described in the following paragraphs. The software's interface is shown in the subsequent methodology sections.

GraphPad Prism 5 (*Graphpad Software LLC, San Diego, USA*) is a software developed for data analysis, providing a myriad of statistical methods for this purpose. Besides organising the data in tables and plotting the respective graphs, it allows curve fitting by linear and non-linear methods with multiple functions as options. It also offers the possibility of comparing differents fits by Akaike information criteria or an F-test, to decide which one mimics better the data behaviour. The parameters of the fittings are displayed along with their absolute errors and their 95% confidence intervals. Additionally, it provides multiple routines to evaluate whether a sample follows a normal probability distribution or not. This software was employed to perform the fitting of the SUV/BW curves and the correspondent fitting parameters allowed the estimation of the TIAC of each organ.

IDAC Dose 2.1. [20] is a program created in 2017 to perform internal dosimetry calculations according to the ICRP-specific absorbed fractions and using the organ of a reference adult as described in ICRP Publication 133 [21]. The software allows the estimation of the organ absorbed doses, as well as the effective doses as described in ICRP Publications 60 and 103 [11, 12], after inserting each organ TIAC as input. The calculation is suported by the radionuclide decay database of ICRP Publication 107 and takes into account 83 different source regions which irradiate 47 target tissues. It also provides an option for calculation of the absorbed dose in spheres with different volumes and composition, which is helpful in radionuclide therapy dosimetry.

OLINDA/EXM 1.0 [22] is also an internal dosimetry computer program, but developed before IDAC DOSE 2.1. The interest of this software for the present work relies on the incorporation of a bladder model that allows the estimation of the bladder's absorbed dose, in a given voiding interval, from the estimated TIAC based on the radioactivity uptake in the urine.

PMOD 4.004 (trial version), PKIN module (*PMOD Technologies LL, Zurich, Switzerland*) [18] was designed for the simulation and fitting of compartment models applied to PET and SPECT data. Time-activity data of the blood plasma and of a given tissue are imported to the program in text file configuration. As an initial aproach, the software fits the time-activity curves and uses them to solve the differential equations associated to the compartment model selected. There are displayed plots with the TACs, the behaviour of the concentration in each compartment and of the total concentration of the model. These results along with the model parameters enable the access to the kinetic behaviour of the radiotracer analysed.

## 3.5 Dose quantification

As an initial approach, mean SUV values of each organ collected from static PET images were corrected for patient body weight and the SUV/BW curves were fitted in the Prism software assuming a least squares ordinary fit. Data points outside the range of three standard deviations from the mean values were excluded and considered as outliers according to the outlier rule of thumb. [23] Single exponential curves with or without a residual were compared by Akaike information criteria whenever possible, and alternatively with an extra sum-of-squares F-test with $p = 0.05$, to inspect which function better described the uptake in each organ. [24] The time-SUV/BW curves were plotted along with their best fitting models and their correspondent 95% confidence intervals.

With the aim of obtaining the TIAC for each organ, the SUV/BW curves were integrated in time from 0 to $\infty$, after applying the correction for the physical decay of $^{68}Ga$. From this operation, TIAC in h/ml were reached and then multiplied by the target masses of the organs in g given in IDAC Dose 2.1. to convert them in h. This operation is allowed because the software assumes that all the organs are composed of water surrogate tissue, i.e., their masses in g correspond to their volumes in ml. Finally, the TIAC in h were used as input in the main menu of IDAC (figure 3.5) to obtain the absorbed doses to the target organs expressed in mGy/MBq as well as the overall effective doses 60 and 103.

Urine activity information was analysed as the cumulative percentage of the injected activity behaviour over time in min. The data points were fitted according to a single exponential cumulative function, i.e., of the type $f(t) = A + B \cdot (1 - e^{-\lambda t})$, where A and B are constants. The TIAC of the urinary bladder was calculated using the MIRD bladder voiding model (15), assuming only one component ($j = 1$) since the activity behaviour was described by a single exponential growth. The parameter $\alpha_1$ was estimated using the constants A and B from the fitting. The bladder TIAC in h was estimated for voiding time intervals $T_\nu$ of 0.5h and 1h. A correction factor of 0.01 was applied in the $\alpha_1$ parameter, since it needed to fall between 0 and 1.

Lastly, the TIAC of the bladder was also calculated in OLINDA/EXM 1.0., to verify the result previously obtained. This software includes the same voiding bladder model in its interface and its filling requirements are the parameters $\alpha_1$, $T_\nu$ and the half-life of the activity being cleared through the urine expressed in h (figure 3.6).

Along the dosimetry process, it was necessary to match the different organs with the source organs and target masses provided by IDAC. This correspondence is illustrated in table 3.5, along with an explanation about how the overall time-activity coefficients of some organs were obtained from the values of their different parts. For most of the organs, the TIAC was calculated taking into account one SUV measurement in the image (1 value). The other TIACs resulted from multiple measurements of SUV in different parts (2 or 3) of the organ in question, being the overall result obtained as the average or the sum of the TIACs associated to the individual parts. The target masses of all irradiated

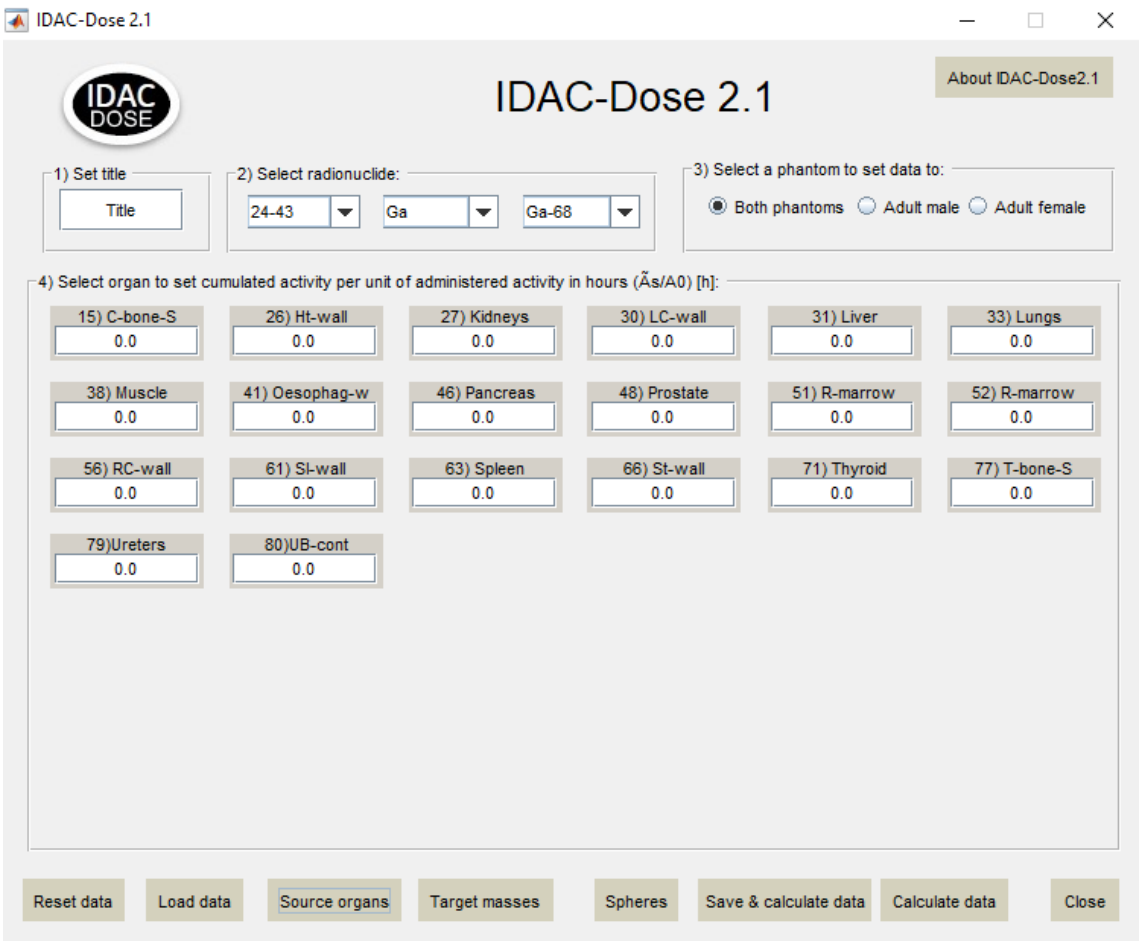


Figure 3.5: IDAC Dose 2.1. interface to insert the TIACs of each organ in h and, consequently, calculate the organ absorbed doses and effective doses for the radionuclide chosen.[20]

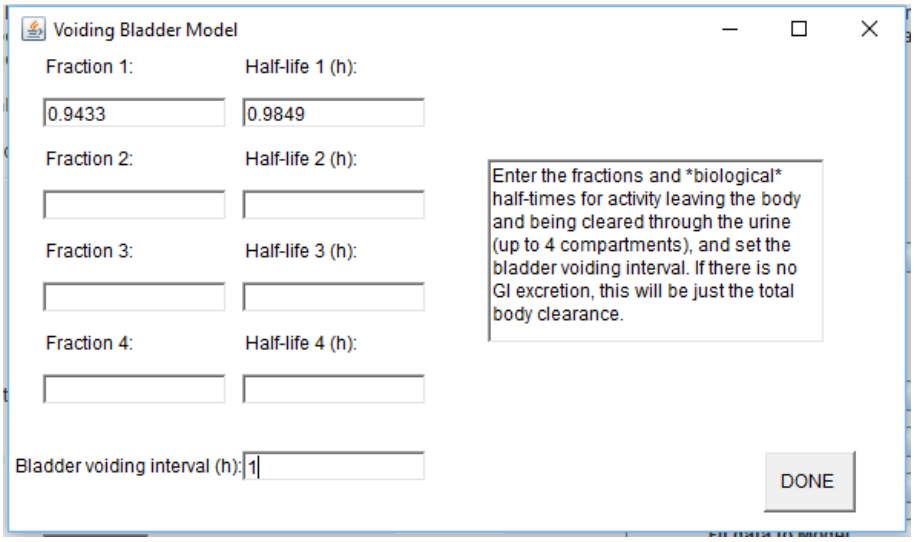


Figure 3.6: OLINDA/EXM 1.0 interface of the voiding bladder model. [22]

organs provided by IDAC is in figure 3.7. It is important to note that the data collected from the blood was treated as uptake in the red bone marrow when using IDAC to calculate the absorbed dose. This procedure is always valid when we are dealing with small molecules and the red bone marrow is expected to experience very low specific uptake. [25] Values from the first time point ($t = 0\ min$) were excluded from the fitting because they were identified as measurements of the background counts.

On this study, SUV values of the nipple, oesophagus (low tract) and rectalfincters were not analysed, as it was not possible to find analogous input in the IDAC interface. These organs were not expected to have a significant uptake, so their omission would not have a relevant impact on the final absorbed dose values.

As a complement, the uncertainty associated with these dosimetry calculations was quantified by the standard error associated to the determined TIAC. Depending on the fitting needed to deduce the TIAC of each organ, the standard error ($SE$) was estimated as follows

$$SE(\tilde{\mathrm{a}}) = \tilde{\mathrm{a}} \cdot \sqrt{\sum_{i=1}^{n} \left(\frac{\sigma_K}{K}\right)^2} \tag{21}$$

where $n$ is the number of independent parameters needed to calculate $\tilde{\mathrm{a}}$, K is the value of each parameter and $\sigma_K$ is its respective standard error. This is a simplication of the covariance matrix, which also takes into account any cross-over influence between parameters on the uncertainty. The individual standard error values are estimated by Prism when the fitting is performed.

In the individual dosimetry analysis, the same method reported previously was employed individually to obtain the fittings for the organs which provided more than two data points. Trapezoidal integration was applied to the data which showed a poor $R^2$ and for the organs that had only two data points. Therefore, the overall time-activity coefficients introduced in IDAC to obtain the absorbed doses were a combination of trapezoidal integration and fitting results.

Individual urinary bladder TIACs were assessed by the same process for 1h voiding. Regarding the red bone marrow dose, the TIACs used in IDAC came from the PET image measurements. It is important to mention that PT7 was excluded in this part of the study, since it was verified he was under prostate medication that would interfere in the dose results.

It must be pointed out that the effective dose estimated using the methods of this section corresponds only to the PET scan. Therefore, there is an additional contribution of dose delivered during the CT scan, which is expected to be around 18 mSv according to the RADAR Medical Procedure Radiation Dose Calculator and assuming a helical CT scan of the chest, abdomen and pelvis. [26]

| **Organs** | **Overall calculation of TIAC** | **IDAC volume match** | **IDAC dose input** |
|---|---|---|---|
| Heart | 1 value | Heart wall | |
| Blood (A, P)[1] | Average | Red (active) bone marrow | |
| Muscle (A, P) | Average | Muscle | |
| Bone (A, P) | Average | Endosteum | 38% Cortical bone surface<br>62% Trabecular bone surface |
| Pancreas<br>(head, mid, tail) | Average | Pancreas | |
| Kidneys (R, L) [2] | Sum | Kidneys | |
| Pyelum (R) | 1 value | Ureters | |
| Lung | 1 value | Lungs | |
| Thyroid | 1 value | Thyroid | |
| Liver | 1 value | Liver | |
| Spleen | 1 value | Spleen | |
| Oesophagus<br>(high, mid) | Average | Oesophagus | |
| Stomach | 1 value | Stomach wall | |
| Intestine | 1 value | Small intestine wall | |
| Colon | Same value for Left/Right Colon | Left colon wall<br>Right colon wall | |
| Rectum | 1 value | Recto-sigmoid colon wall | |
| Prostate | 1 value | Prostate | |
| Urine | 1 value | ———— | Urinary bladder contents |

Table 3.5: Target organs and respective IDAC volumes and dose inputs.

[1] Abdominal and pelvic measurements
[2] Right, Left

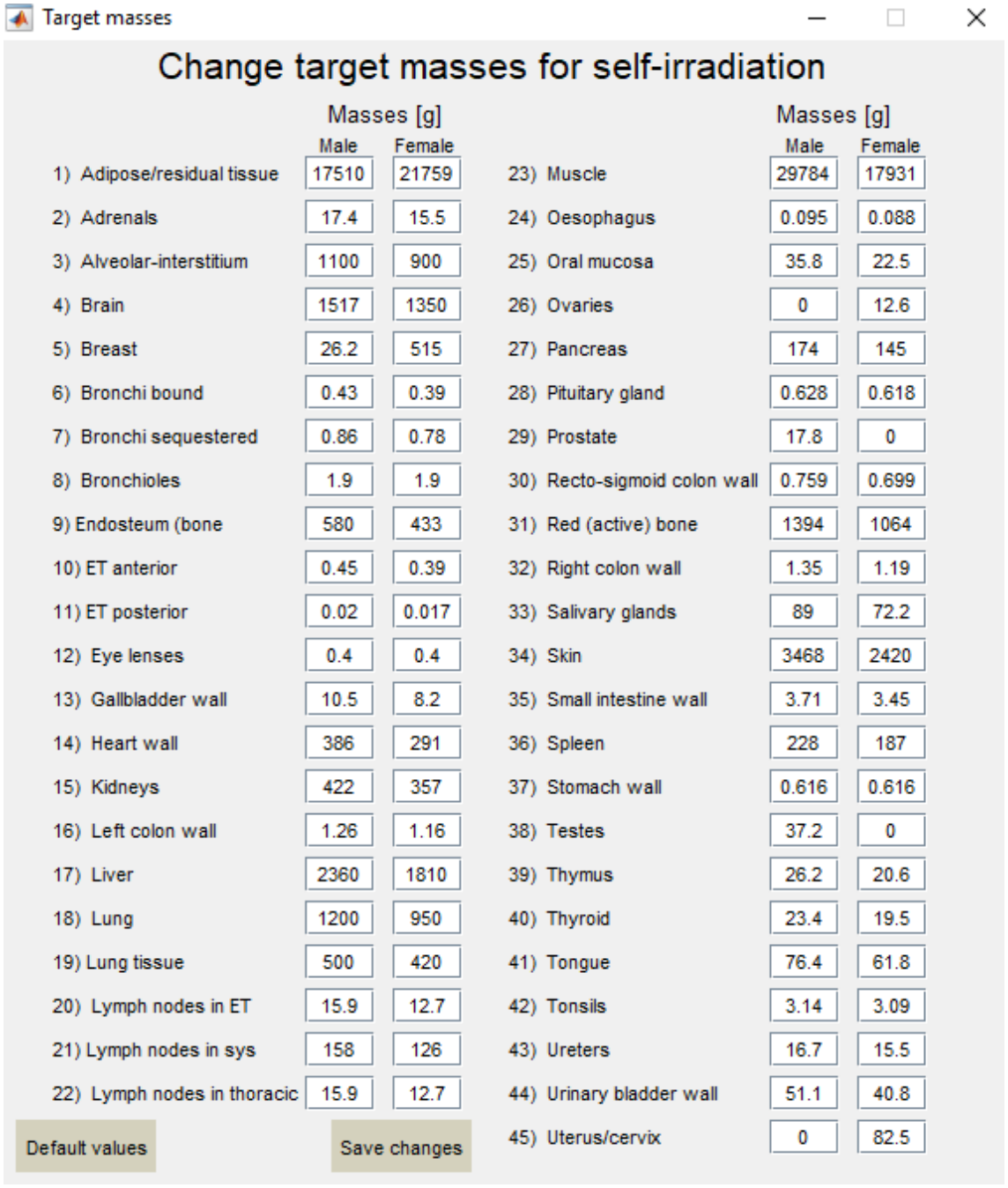


Figure 3.7: Target masses of all possible irradiated organs provided IDAC. [20]

## 3.6 Pharmacokinetic analysis

The pharmacokinetic analysis with the application of compartmental modelling is based on the time-activity curve of the arterial plasma, also designated as Arterial Input Function (AIF), and on the time-activity curve of a given tissue, both including dynamic and static data. This analysis was performed only for patients 2 and 11 individually, since the AIFs of the other patients were strongly scattered at early time points and, when inserted in the PMOD software, led to inconclusive results when estimating the compartimental curve's behaviour and respective parameters.

In the first place, to import the time-activity curves of the plasma and the tissue into PMOD, the user manual establishes that this information should be presented in a text file, with the time points in seconds and the activity points in kBq/cc (kilobecquerel per cubic centimeter). Since the activity is first expressed by the SUV, a conversion to kBq/cc was required, which involved using the actual injected activity and body weight of the patient being analysed, according to equation (1).

The remainder steps were the simplest, due to the user-friendly interface of PMOD PKIN module (figure 3.8). On bottom left corner of the window, there is the "kinetic" with options to import the text files with the activity data from both plasma and tissue. On the top right corner of the window, we can select the compartment model to perform the fitting. The parameters of the model appear right below, along with the respective standard error. Two graphs of strong relevance are also displayed. The first one on the top left corner includes both activity curves (plasma and tissue) together with the model curve ($C_{model}$). The other one on the bottom right corner presents the behaviour of the concentration in the tissue compartments also with the model curve ($C_{model}$). There is the option of showing other behaviours in the graphs, but the ones described here were thought to be the most important.

Another point worth noting is that, in this situation, the tissue is either the tumour or the normal prostate. A two-tissue compartment model was applied for the tumour of both patients and for the normal prostate tissue for patient 11. This healthy tissue was also examined using a one-tissue compartment model for comparison purposes.

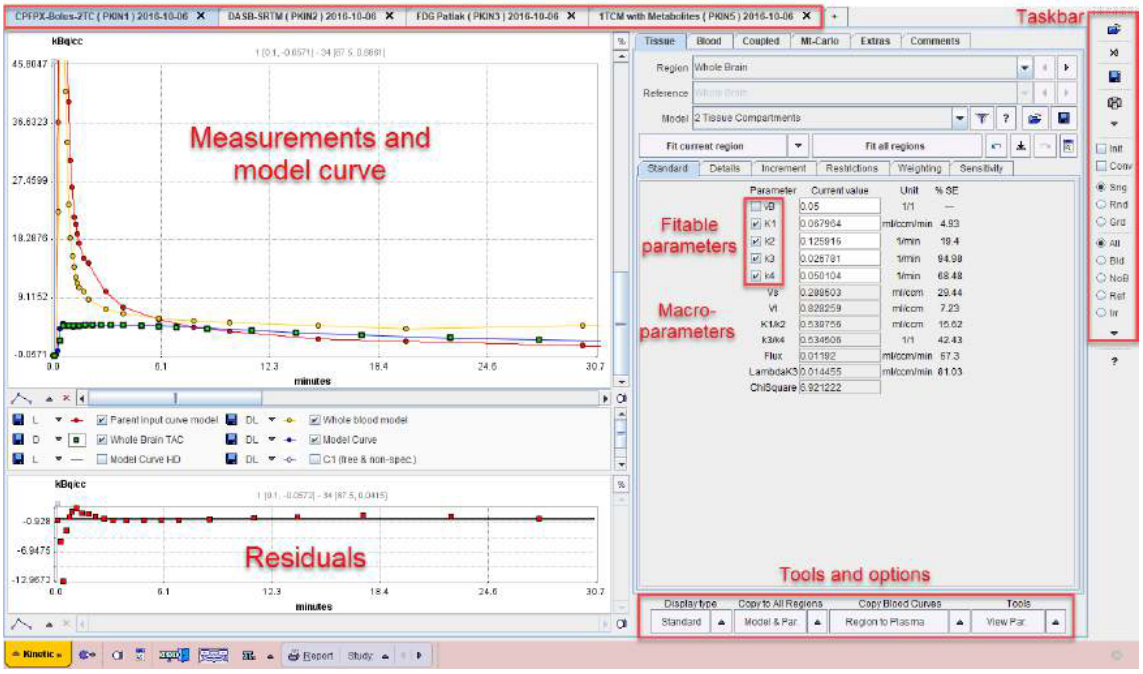


Figure 3.8: PMOD PKIN module interface. [18]

# 4 Radionuclide therapy

## 4.1 Lutetium-177 in targeted radionuclide therapy

Lutetium-177 ($^{177}$Lu) decays 100% by $\beta^-$ emission, but it is not a pure beta emitter according to the decay scheme shown in figure 4.1. Most of the disintegrations of this radionuclide (79.3%) are into stable isotopes of hafnium-177 ($^{177}$Hf) with a half-life of 6.647 days, followed by less frequent decay events for excited states. Subsequent de-excitation for the ground state of $^{177}$Hf is accompanied by photon emission. Thus, in the radioactive decay of $^{177}$Lu, the main particle emission events are of $\beta^-$ particles with energies 498 keV, 385 keV and 177 keV, as well as low-energy gamma photons of 113 keV and 208 keV.

There are many characteristics of $^{177}$Lu that explain the increasing application of this radioisotope in targeted radionuclide therapy. In the first place, the electrons released during decay (including Auger electrons) experience a mean penetration range of 670 $\mu$m in soft tissue, which allows the erradication of small tumours or metastasis while sparing the surrounding normal tissues. At the same time, the low-energy gamma photons emitted enable treatment control through imaging techniques, as well as dosimetric and kinetic studies before and during treatment, which contributes for a personalized medicine approach. Since the beta particles and the photons emitted are of average and low energy, respectively, they are associated to relatively low levels of radiation, which simplifies the labelling process to obtain the radiopharmaceuticals and their administration to the pa-

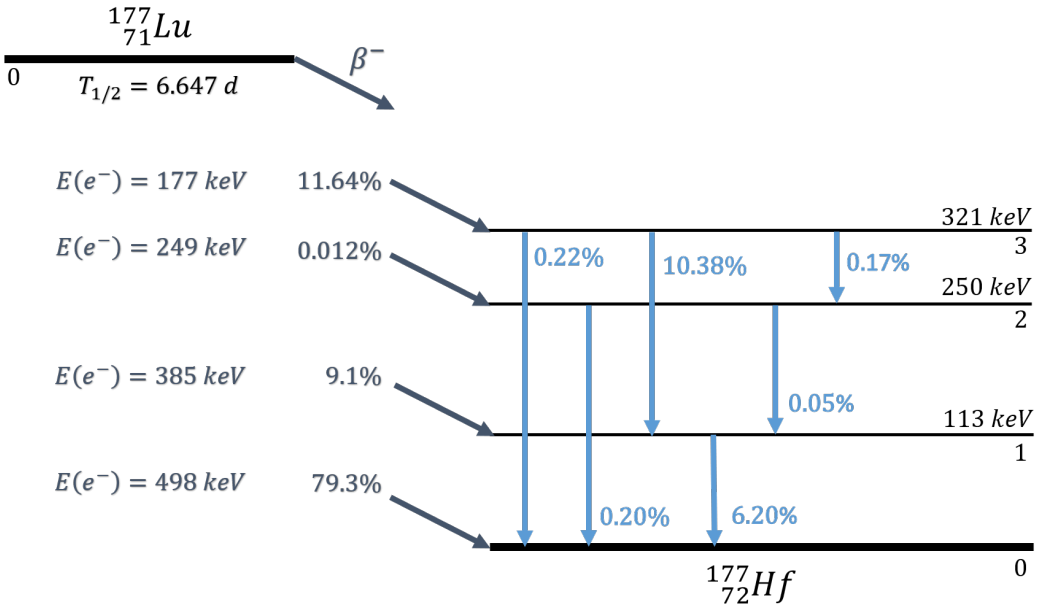


Figure 4.1: Decay scheme of $^{177}$Lu. [6]

tients. In a chemical point of view, there is labelling compatibility with several molecules, including peptides, proteins and antibodies depending on the target organ. As it is a longer-lived radionuclide, $^{177}$Lu demonstrated to be particularly suitable for antibody labelling, since these molecules tend to demonstrate slower kinetic properties. At last instance, its longer half-life contributes to reduce activity losses during transportation between production and medical facilities, as well as between the storage and the patients' rooms for further injection.

The production of $^{177}$Lu for medical applications involves a nuclear reactor and can be performed by two different methods (figure 4.2). The direct method requires neutron irradiation of $^{176}$Lu targets, in which $^{177}$Lu is created along with photon emission. The second production method is indirect and relies, in the first place, on neutron irradiation of ytterbium-176 ($^{176}$Yb) targets, producing $^{177}$Yb that experiences $\beta^-$ decay into $^{177}$Lu. At this point, a chemical separation procedure is needed to remove the $^{176}$Yb target atoms. The advantage of this carrier-free route is that it yields higher specific activities and no production of $^{177m}$Lu.

After obtaining the radioisotopes and before the preparation of the desired radiopharmaceuticals, quality control operations take place to evaluate $^{177}$Lu purity, a property that has a large influence on its specific activity. In a particular application, the number of target receptors determines the amount of $^{177}$Lu specific activity that is needed to be incorporated in the radiotracer. At this point, many $^{177}$Lu radioagents have been produced and analysed to be applied in several terapeutic procedings such as peptide receptor radionuclide therapy, bone pain palliation, radiation synovectomy and radioimmunotherapy.

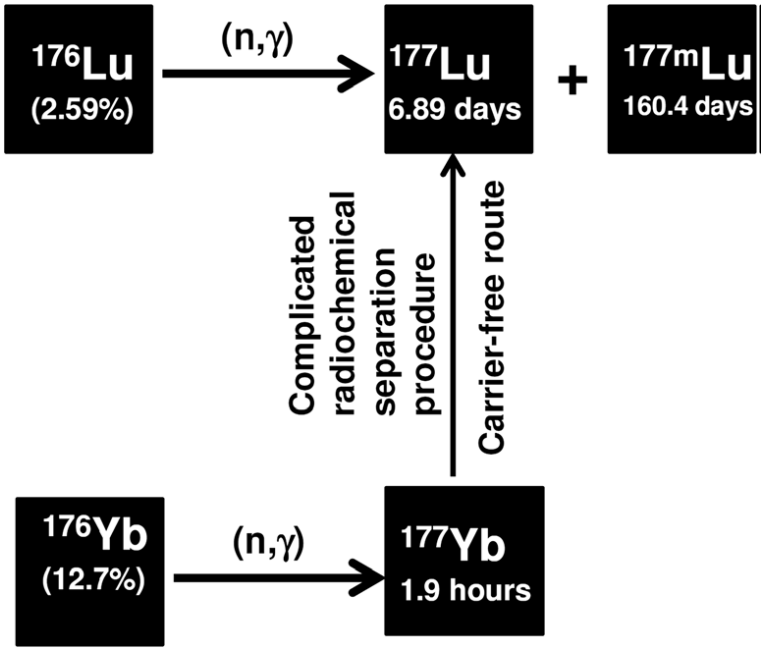


Figure 4.2: Methods employed in reactor production of $^{177}$Lu.[27]

## 4.2 Normal organ dosimetry

It was already recognized that the potential organs at risk in imaging with a GRPR antagonist are the pancreas and the kidneys. In therapeutic circumstances, quantifying the dose delivered to the red bone marrow is also of strong importance to avoid future permanent damage. Therefore, the possibility of using [$^{177}$Lu]SB3 as a therapy agent was evaluated, estimating its absorbed dose to the pancreas, kidneys and red bone marrow based on the obtained decay of [$^{68}$Ga]SB3 in these organs.

In first instance, the biological half-life of [$^{177}$Lu]SB3 was assumed to be equal to the biological half-life of [$^{68}$Ga]SB3. Subsequently, it was estimated the effective decay constant of [$^{177}$Lu]SB3 in the pancreas, keeping in mind equations (12) and (13) and the same analysis performed by Gnesin *et al*. [28] The TIAC in h/ml was obtained, considering that the SUV/BW curve in time for the pancreas follows a single exponential decay without residual. TIACs and respective absorbed doses (in Gy/GBq) were obtained for each patient pancreatic volume, as well as for the average and phantom pancreas volumes.

It was possible to estimate the individual volumes of the pancreas from the PET images. Moreover, IDAC provides a S-value for an adult male standard pancreas volume after selecting a pancreas TIAC of 1h in the main menu. This S-value allows to make a prediction on the S-value for each individual pancreas volume assuming a linear relation between these quantities. Finally, absorbed doses to the pancreas were also quantified for an administered activity of 7.4 GBq, which is the typical activity amount injected in prostate cancer therapy with other $^{177}$Lu radiolabelled agents.

The evaluation of the [$^{177}$Lu]SB3 absorbed dose to the kidneys relies on the same calculation method as for the pancreas. However, some different aspects should be noted. In this case, the TIAC in h/ml was estimated for each kidney part involved, i.e., right and left kidney cortexes and right pyelum (kidney pelvis). Cortex TIAC values were added and multiplied by the volume in ml of both kidneys in the reference male phantom. As mentioned in table 3.5, the pyelum was treated as an ureters surrogate, so its TIAC was determined using the reference male ureters volume in ml.

The absorbed dose to the red bone marrow was assessed in the same way but only for the respective reference volume in the male phantom. The fitting parameters of the blood sample curve were used in this case, since they are expected to give more accurate results and to provide a higher TIAC, which would result in a higher absorbed dose.

Quantifying this systematic error involved the 95% confidence intervals associated to the Prism fitting parameters for these organs. The calculation is performed in the same as described earlier in this section but using the upper and lower limits of the 95% confidence intervals of the biological decay constant of the organ to obtain the absorbed doses. It should be pointed out that the biological decay constant and the correspondent absorbed dose are inversely related, i.e. the lower limit of the 95% confidence interval

corresponds to a higher dose and vice-versa. In the end, it was possible to determine an extra dose range that would remain in each target organ.

## 4.3 Tumour and normal prostate dosimetry

In this section, a review on the methodology used to estimate the $^{177}$Lu absorbed dose to a particular tumour is presented. First of all, the tumour SUV/BW curve, including dynamic and static data, was fitted in Prism. A function of the type $f(t) = A \cdot (e^{-\lambda_1 t} - e^{-\lambda_2 t})$ ($A$ is a constant) was found to be the most suitable to mimic the data behaviour, which is typical of an uptake and excretion curve. In the fitting parameters, there was an estimation of the biological half-life of the tumour and, together with the physical half-life of $^{177}$Lu, a quantification of the tumour's TIAC in h/ml was achieved.

In a situation in which the measurement of tumour volume is not possible, it can be created a range of volumes, whose upper limit is the volume of the prostate in the male phantom. Those volumes are required to obtained the TIACs in h. Hereafter, it was calculated the time-integrated activity Ã in MBq·h for each volume, according to equation (10) and assuming the standard injected activity of 7.4 GBq.

To quantify the absorbed dose to the tumour, the $^{177}$Lu S-values associated to each tumour volume are required. They are easily found in a table of the IDAC spheres mode, selecting a cumulated activity of 1.0 MBq· h (figure 4.3). A plot of S-values times volume in mGy·ml/(MBq·h) as a function of volume was created. A logarithmic behaviour was the most accurate to fit the data. Using the logarithmic equation, it was possible to estimate the values of S-value of each volume. The correspondent absorbed doses were obtained with expression (7).

Unfortunately, such small volumes are prone to suffer from PVE during the $^{68}$Ga imaging procedure, which results in an underestimation of their radioactivity. Therefore, the estimated absorbed doses should be corrected taking this fact into account. One way to perform the correction is employing recovery coefficients characteristic of $^{68}$Ga imaging. These coefficients are displayed as a function of the diameter of the objects being scanned in a paper written by A. Sanchez-Crespo [7]. In view of this, the absorbed doses PVE corrected can be assessed dividing the doses values already determined by the correspondent recovery coefficients.

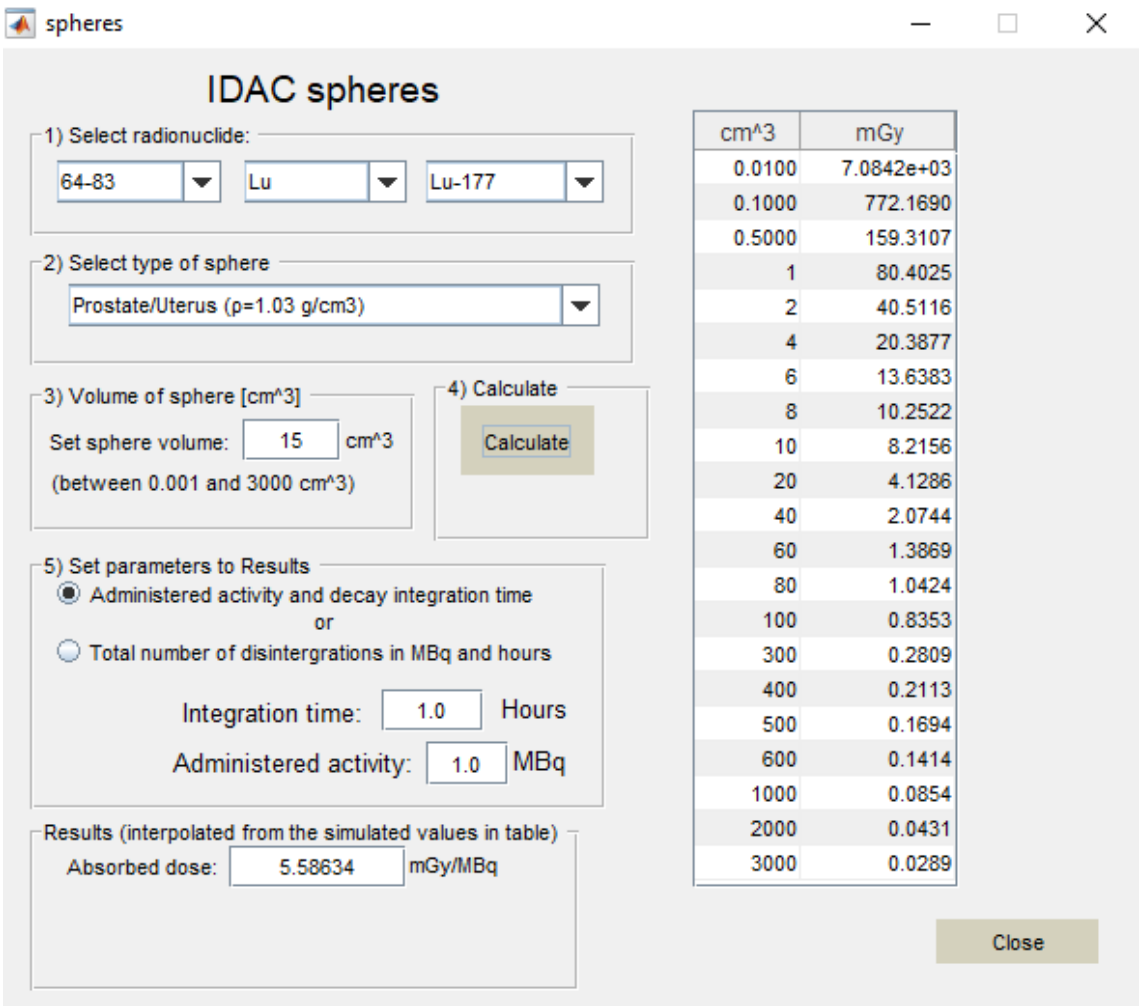


| cm^3 | mGy |
|---|---|
| 0.0100 | 7.0842e+03 |
| 0.1000 | 772.1690 |
| 0.5000 | 159.3107 |
| 1 | 80.4025 |
| 2 | 40.5116 |
| 4 | 20.3877 |
| 6 | 13.6383 |
| 8 | 10.2522 |
| 10 | 8.2156 |
| 20 | 4.1286 |
| 40 | 2.0744 |
| 60 | 1.3869 |
| 80 | 1.0424 |
| 100 | 0.8353 |
| 300 | 0.2809 |
| 400 | 0.2113 |
| 500 | 0.1694 |
| 600 | 0.1414 |
| 1000 | 0.0854 |
| 2000 | 0.0431 |
| 3000 | 0.0289 |

Figure 4.3: IDAC Dose 2.1. spheres sub-module interface for tumour dosimetry. [20]

# 5 Results and discussion

## 5.1 Biodistribution of [$^{68}$Ga]SB3

The biodistribution of [$^{68}$Ga]SB3 within the 10 patients is shown in figure 5.1, along with the ratio between the administered activity and the body weight in MBq/kg. There is a strong evidence of a high and homogeneous tracer uptake in the pancreas, in addition to the excretion of the radiopharmaceutical through the renal pelvis, ureters and urinary bladder. Patient 7 is not encountered in this representation.

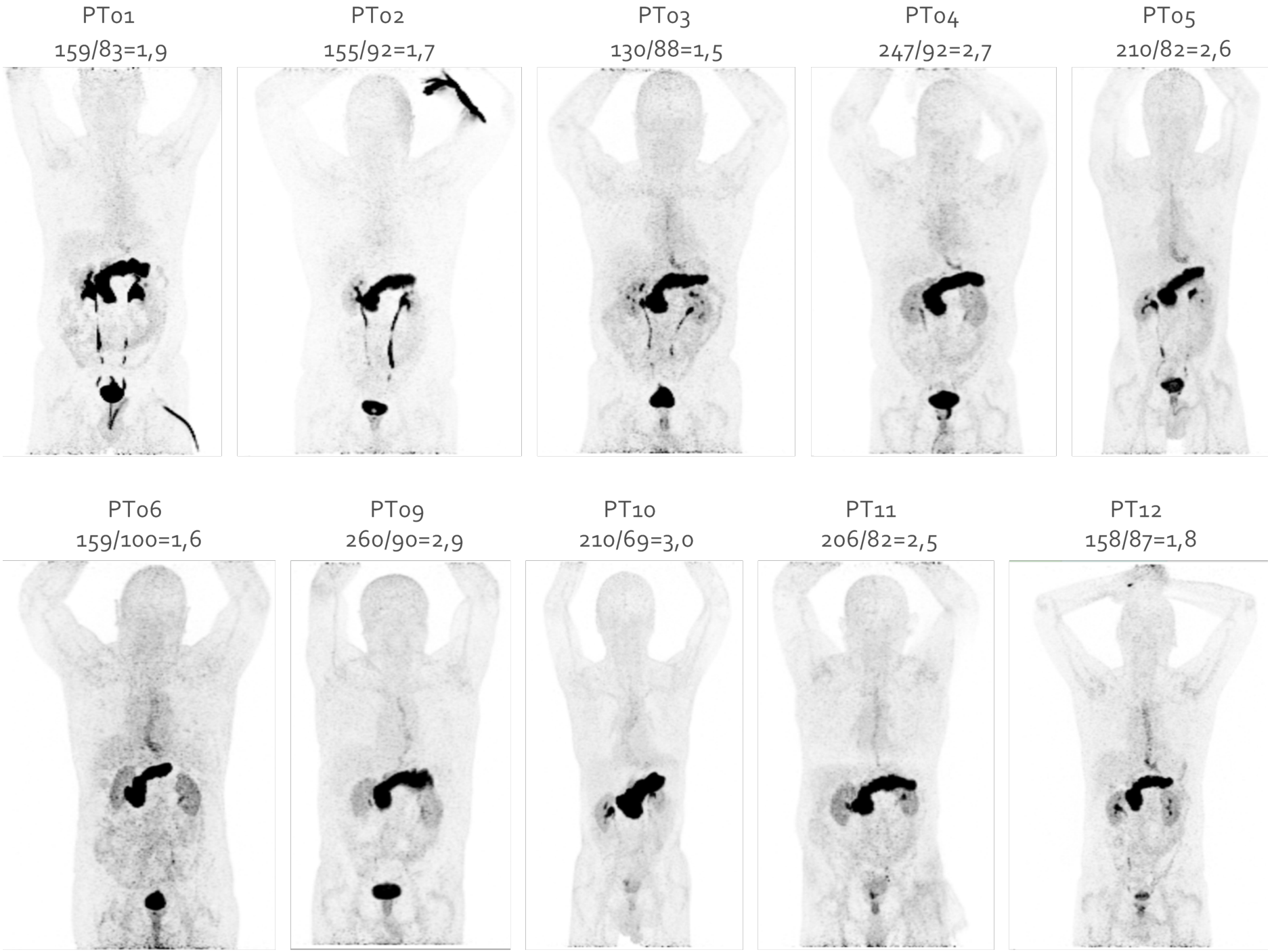


Figure 5.1: Individual biodistribution of [$^{68}$Ga]SB3 along with the ratio between the administrated activity and body weight in MBq/kg. [29]

## 5.2 Average dosimetry of [$^{68}$Ga]SB3

Curves of the SUV/BW as a function of time are represented in figure 5.2 for the most important organs, as well as the tracer uptake in the urine. The estimated TIACs after integration and their standard error are indicated in 5.1. In table 5.2, organ absorbed doses and effective doses 60 and 103 are reported for voiding intervals of 0.5h and 1h. Here, the red bone marrow absorbed dose was estimated with the TIAC obtained from the PET image data. However, in intermediate calculations, it was noticed that the TIAC for the red bone marrow was three times higher if estimated from the gamma counter blood data, which would result in a higher dose to the bone marrow and, consequently, a higher effective dose. Nevertheless, these changes in dose were not significant, since the bone marrow is not expected to have a considerable uptake of the radiopharmaceutical, as seen in the reported biodistribution (figure 5.1).

The organs that receive the highest absorbed dose are the pancreas (198 $\mu$Gy/MBq), the kidney pelvis (133 $\mu$Gy/MBq), the urinary bladder wall (115 $\mu$Gy/MBq) and the kidney cortex (53 $\mu$Gy/MBq) for a 1h voiding interval. Effective dose 60 and 103 values of 15 $\mu$Sv/MBq and 13 $\mu$Sv/MBq were obtained, respectively. The reduction of the voiding interval to 30 min produces lower absorbed dose values in following organs: small intestine wall (-22%), colon wall (-23%), rectum (-43%), prostate (-32%) and urinary bladder wall (-49%). There is also a decrease in the effective doses 60 (-22%) and 103 (-23%). This behaviour is expected since these organs are near or belong to the urinary tract and the radioactivity remains in the urine for a shorter period.

A recent published paper on dosimetry for the bombesin analogue [$^{68}$Ga]-NODAGA-M19 shows similar values for the organ absorbed doses and effective dose 103 for a voiding interval of 1h. Nevertheless, [$^{68}$Ga]SB3 yields lower absorbed dose in the pancreas, liver and spleen, as well as a lower effective dose 103. On the other hand, a higher absorbed dose is observed in the urinary bladder wall, prostate and kidneys. [28] Although in the same order of magnitude, the effective dose 103 of [$^{68}$Ga]SB3 appears to be slightly lower than the ones reported for the most commonly used radiopharmaceuticals in nuclear medicine diagnostic procedures ([$^{18}$F]FDG, [$^{68}$Ga]PSMA, [$^{68}$Ga]DOTA-TATE, [$^{68}$Ga]DOTA-NOC, [$^{68}$Ga]DOTA-TOC). [2]

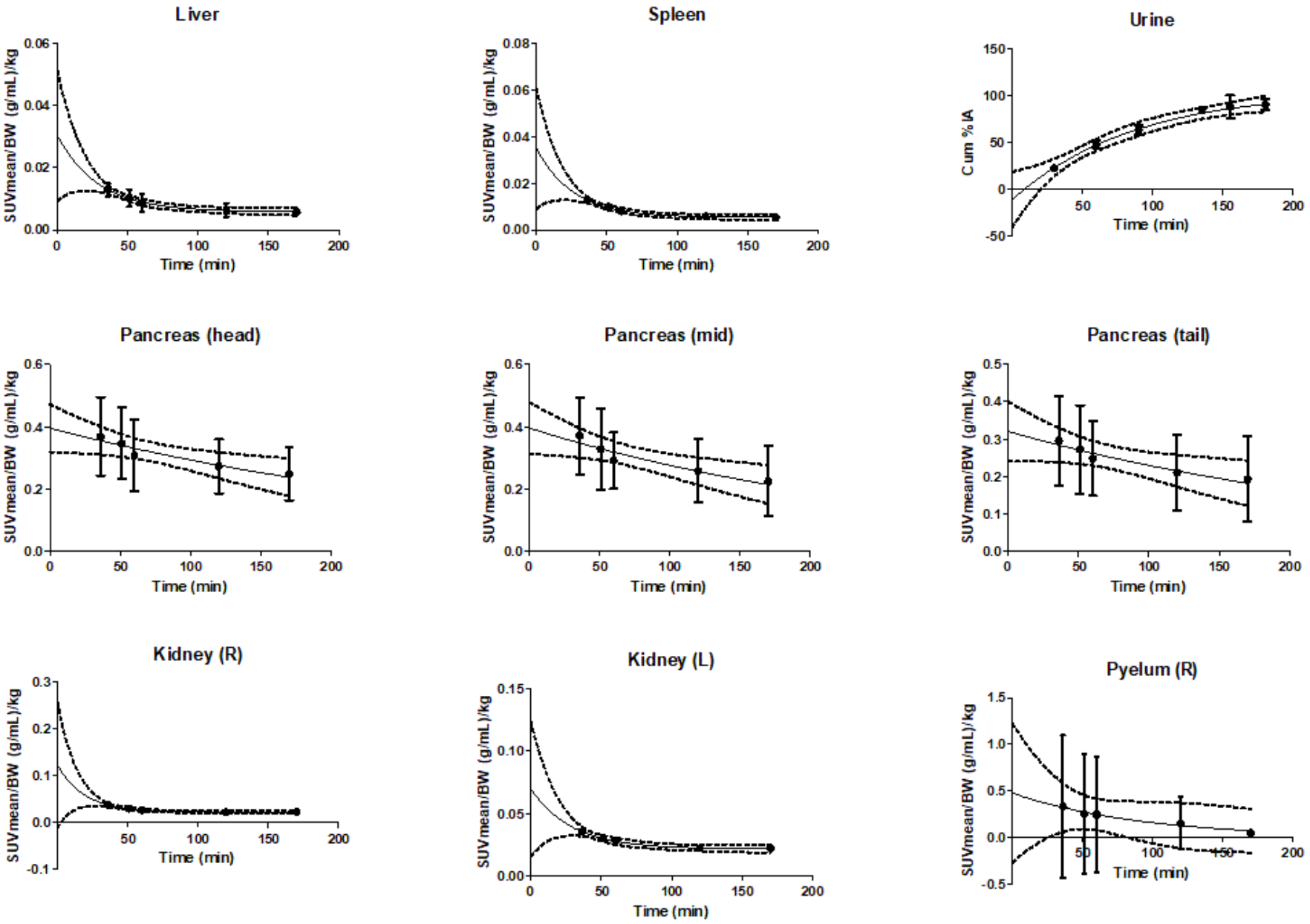


Figure 5.2: SUV/BW in (g/ml)/kg as a function of time in min for the most important organs. The uptake in the urine is represented in a cumulative percentage of the injected activity (Cum %IA).

| Target organs | TIAC (h) | Standard Error |
|---|---|---|
| Heart wall | 6,55E-03 | 3,65E-03 |
| Red bone marrow[3] | | |
| | 3,20E-02 | 7,57E-03 |
| | 9,45E-02 | 2,40E-02 |
| Lung | 5,89E-03 | 4,18E-03 |
| Muscle | 1,83E-01 | 6,93E-02 |
| Cortical bone surface | 6,55E-03 | 1,67E-03 |
| Trabecular bone surface | 2,91E-03 | 1,21E-03 |
| Thyroid | 3,42E-04 | 1,36E-04 |
| Liver | 4,39E-02 | 2,15E-02 |
| Spleen | 4,37E-03 | 2,12E-03 |
| Pancreas | 7,94E-02 | 3,35E-02 |
| Pyelum | 7,75E-03 | 1,46E-02 |
| Kidneys | 4,82E-02 | 3,10E-02 |
| Oesophagus | 2,35E-06 | 1,41E-06 |
| Stomach wall | 7,00E-06 | 1,10E-05 |
| Small intestine wall | 6,60E-05 | 2,62E-05 |
| Colon wall | 2,15E-05 | 9,95E-06 |
| Recto-sigmoid colon wall | 2,00E-05 | 9,29E-06 |
| Prostate | 1,75E-05 | 1,57E-05 |
| Urinary bladder contents[4] | | |
| | 4,45E-04 | 6,00E-05 |
| | 1,26E-01 | 7,78E-02 |

Table 5.1: TIAC of the targeted organs in h and respective standard error.

[3] Image and blood sample values.
[4] 0.5h and 1h voiding interval.

| | 0.5h voiding | 1h voiding |
|---|---|---|
| **Target organs** | **Dose (mGy/MBq)** | **Dose (mGy/MBq)** |
| Heart wall | 7,92E-03 | 7,94E-03 |
| Red bone marrow | 6,73E-03 | 7,38E-03 |
| Lung | 3,21E-03 | 3,23E-03 |
| Muscle | 3,80E-03 | 4,12E-03 |
| Endosteum | 3,72E-03 | 4,08E-03 |
| Thyroid | 6,12E-03 | 6,12E-03 |
| Liver | 1,22E-02 | 1,22E-02 |
| Spleen | 1,04E-02 | 1,04E-02 |
| Pancreas | 1,98E-01 | 1,98E-01 |
| Pyelum | 1,31E-01 | 1,33E-01 |
| Kidneys | 5,24E-02 | 5,25E-02 |
| Oesophagus | 2,20E-03 | 2,22E-03 |
| Stomach wall | 5,03E-03 | 5,09E-03 |
| Small intestine wall | 4,93E-03 | 6,30E-03 |
| Colon wall | 3,37E-03 | 4,35E-03 |
| Recto-sigmoid colon wall | 5,32E-03 | 9,40E-03 |
| Prostate | 2,00E-02 | 2,92E-02 |
| Urinary bladder wall | 5,92E-02 | 1,15E-01 |
| Effective dose 60 (mSv/MBq) | 1,15E-02 | 1,47E-02 |
| Effective dose 103 (mSv/MBq) | 9,95E-03 | 1,29E-02 |

Table 5.2: Organs absorbed doses in mGy/MBq and effective doses in mSv/MBq for a 0.5h and 1h voiding interval, including the image blood values.

## 5.3 Individual dosimetry of [$^{68}$Ga]SB3

Individual TIACs are presented in table 5.3, followed by the respective organ absorbed doses and effective doses 60 and 103 shown in table 5.4. Average and standard deviation of these quantities are displayed in 5.5. Since the pancreas behavior did not follow a normal probability distribution, its statistics was described by the mean, median, maximum and minimum values in table 5.6. In these results, it is clear the diference in response to [$^{68}$Ga]SB3 from patient to patient, despite having been all previously diagnosed with the same pathology.

| | TIAC (h) | | | | | | | | | |
|---|---|---|---|---|---|---|---|---|---|---|
| **Target organs** | **PT1** | **PT2** | **PT3** | **PT4** | **PT5** | **PT6** | **PT9** | **PT10** | **PT11** | **PT12** |
| Muscle | 1,56E-01 | 5,92E-02 | 1,69E-01 | 2,02E-01 | 2,03E-01 | 2,50E-01 | 1,42E-01 | 2,03E-01 | 1,61E-01 | 1,56E-01 |
| Cortical bone surface | 3,91E-06 | 8,49E-07 | 2,55E-06 | 3,20E-06 | 3,29E-06 | 6,69E-06 | 2,87E-06 | 2,47E-06 | 2,78E-06 | 2,91E-06 |
| Trabecular bone surface | 6,38E-06 | 1,39E-06 | 4,17E-06 | 5,22E-06 | 5,37E-06 | 1,09E-05 | 4,68E-06 | 4,03E-06 | 4,54E-06 | 4,74E-06 |
| Liver | 3,10E-02 | 7,57E-04 | 2,93E-02 | 2,49E-02 | 3,87E-02 | 4,59E-02 | 2,99E-02 | 4,06E-02 | 4,34E-02 | 3,20E-02 |
| Spleen | 3,35E-03 | 3,03E-05 | 2,20E-04 | 3,00E-03 | 3,59E-03 | 4,04E-03 | 3,25E-03 | 4,13E-03 | 3,19E-03 | 3,20E-03 |
| Pancreas | 9,21E-02 | 3,43E-03 | 2,80E-02 | 8,44E-02 | 1,95E-01 | 6,28E-01 | 1,29E-01 | 8,94E-01 | 6,28E-02 | 7,75E-02 |
| Kidneys | 4,38E-02 | 2,00E-04 | 3,88E-02 | 4,01E-02 | 2,68E-01 | 4,19E-02 | 2,62E-01 | 3,92E-01 | 3,96E-01 | 1,69E-01 |
| Pyelum | 4,96E-02 | 1,92E-04 | 2,69E-04 | 7,04E-04 | 2,67E-02 | 5,92E-04 | 8,70E-04 | 2,76E-02 | 1,12E-02 | 1,65E-02 |
| Stomach wall | 4,39E-06 | 6,61E-09 | 9,71E-07 | 4,67E-06 | 7,58E-06 | 6,49E-05 | 6,43E-05 | 7,84E-05 | 1,31E-04 | 6,37E-06 |
| Small intestine wall | 5,85E-05 | 2,07E-06 | 7,03E-05 | 4,24E-05 | 7,13E-05 | 9,01E-04 | 5,63E-04 | 6,19E-04 | 5,53E-04 | 8,16E-05 |
| Right colon wall | 1,72E-05 | 6,90E-07 | 2,11E-06 | 1,77E-05 | 1,96E-05 | 1,98E-04 | 1,44E-04 | 2,28E-04 | 1,97E-04 | 3,07E-04 |
| Left colon wall | 1,61E-05 | 6,44E-07 | 1,97E-06 | 1,65E-05 | 1,83E-05 | 1,85E-04 | 1,35E-04 | 2,12E-04 | 1,84E-04 | 2,86E-04 |
| Recto-sigmoid colon wall | 1,76E-05 | 6,73E-06 | 1,95E-05 | 2,28E-05 | 2,20E-05 | 2,82E-05 | 1,80E-05 | 2,19E-05 | 1,56E-05 | 2,45E-05 |
| Prostate | 3,71E-04 | 3,33E-04 | 4,15E-04 | 1,13E-03 | 5,01E-04 | 4,87E-04 | 3,58E-04 | 4,64E-04 | 5,10E-04 | 5,59E-04 |
| Heart | 3,23E-03 | 1,26E-03 | 4,86E-03 | 4,84E-03 | 5,21E-03 | 7,34E-03 | 3,87E-03 | 5,81E-03 | 3,23E-03 | 3,72E-03 |
| Lung | 2,05E-03 | 1,02E-03 | 3,56E-03 | 6,12E-03 | 4,11E-03 | 6,92E-03 | 5,52E-03 | 2,84E-03 | 2,79E-03 | 3,46E-03 |
| Thyroid | 1,60E-04 | 8,26E-05 | 2,48E-04 | 2,66E-04 | 2,82E-04 | 2,22E-04 | 2,26E-04 | 2,79E-04 | 1,53E-04 | 2,03E-04 |
| Oesophagus | 1,40E-06 | 6,87E-07 | 1,60E-06 | 1,55E-06 | 1,84E-06 | 2,09E-06 | 1,74E-06 | 1,98E-06 | 1,81E-06 | 1,95E-06 |
| Red bone marrow | 2,19E-02 | 1,24E-02 | 9,22E-02 | 3,26E-02 | 3,56E-02 | 3,96E-02 | 3,13E-02 | 3,11E-02 | 3,96E-02 | 3,33E-02 |
| Urinary bladder contents | 2,46E-01 | 2,11E-01 | 1,37E-01 | 2,50E-01 | 1,44E-01 | 1,89E-01 | 2,61E-01 | 2,50E-01 | 2,91E-01 | 3,04E-01 |

Table 5.3: Individual TIACs in h.

| | Dose (mGy/MBq) | | | | | | | | | |
|---|---|---|---|---|---|---|---|---|---|---|
| **Target organs** | **PT1** | **PT2** | **PT3** | **PT4** | **PT5** | **PT6** | **PT9** | **PT10** | **PT11** | **PT12** |
| Muscle | 3,75E-03 | 1,58E-03 | 3,62E-03 | 4,38E-03 | 4,84E-03 | 5,84E-03 | 3,91E-03 | 6,31E-03 | 4,59E-03 | 4,07E-03 |
| Endosteum | 3,69E-03 | 1,55E-03 | 7,09E-03 | 4,14E-03 | 4,73E-03 | 6,16E-03 | 3,80E-03 | 6,04E-03 | 5,17E-03 | 4,46E-03 |
| Liver | 9,68E-03 | 4,87E-04 | 8,05E-03 | 8,18E-03 | 1,62E-02 | 2,40E-02 | 1,27E-02 | 3,25E-02 | 1,60E-02 | 1,11E-02 |
| Spleen | 8,46E-03 | 3,43E-04 | 2,20E-03 | 7,71E-03 | 1,32E-02 | 1,38E-02 | 1,18E-02 | 2,11E-02 | 1,34E-02 | 1,00E-02 |
| Pancreas | 2,29E-01 | 8,79E-03 | 7,09E-02 | 2,09E-01 | 4,86E-01 | 1,55E+00 | 3,23E-01 | 2,21E+00 | 1,63E-01 | 1,95E-01 |
| Kidneys | 4,86E-02 | 6,53E-04 | 4,17E-02 | 4,39E-02 | 2,81E-01 | 5,51E-02 | 2,73E-01 | 4,20E-01 | 4,10E-01 | 1,77E-01 |
| Pyelum | 8,16E-01 | 6,86E-03 | 8,96E-03 | 1,81E-02 | 4,46E-01 | 2,18E-02 | 2,52E-02 | 4,72E-01 | 1,96E-01 | 2,79E-01 |
| Stomach wall | 5,36E-03 | 4,17E-04 | 2,65E-03 | 4,88E-03 | 1,15E-02 | 2,75E-02 | 8,59E-03 | 4,11E-02 | 7,40E-03 | 5,78E-03 |
| Small intestine wall | 7,80E-03 | 2,70E-03 | 3,61E-03 | 6,11E-03 | 1,08E-02 | 1,94E-02 | 9,48E-03 | 3,06E-02 | 9,94E-03 | 8,24E-03 |
| Colon wall | 4,65E-03 | 1,96E-03 | 2,75E-03 | 4,22E-03 | 7,01E-03 | 1,07E-02 | 6,78E-03 | 1,75E-02 | 7,72E-03 | 6,07E-03 |
| Recto-sigmoid colon wall | 9,63E-03 | 7,41E-03 | 5,86E-03 | 9,52E-03 | 6,56E-03 | 8,22E-03 | 9,92E-03 | 1,09E-02 | 1,12E-02 | 1,15E-02 |
| Prostate | 2,76E-02 | 2,34E-02 | 2,04E-02 | 4,41E-02 | 2,30E-02 | 2,62E-02 | 2,83E-02 | 3,05E-02 | 3,40E-02 | 3,59E-02 |
| Heart | 4,58E-03 | 1,44E-03 | 6,01E-03 | 6,16E-03 | 8,02E-03 | 1,21E-02 | 6,15E-03 | 1,31E-02 | 5,74E-03 | 5,44E-03 |
| Lungs | 1,90E-03 | 5,54E-04 | 2,46E-03 | 3,11E-03 | 3,63E-03 | 5,50E-03 | 3,50E-03 | 5,84E-03 | 3,06E-03 | 2,62E-03 |
| Thyroid | 3,18E-03 | 1,51E-03 | 4,87E-03 | 4,98E-03 | 5,44E-03 | 4,90E-03 | 4,32E-03 | 5,88E-03 | 3,36E-03 | 3,95E-03 |
| Oesophagus | 1,78E-03 | 3,80E-04 | 2,08E-03 | 1,98E-03 | 3,43E-03 | 5,33E-03 | 2,71E-03 | 7,43E-03 | 2,98E-03 | 2,23E-03 |
| Red bone marrow | 6,32E-03 | 3,00E-03 | 1,43E-02 | 7,39E-03 | 9,04E-03 | 1,11E-02 | 8,00E-03 | 1,27E-02 | 1,01E-02 | 8,31E-03 |
| Urinary bladder wall | 1,15E-01 | 9,81E-02 | 6,47E-02 | 1,17E-01 | 6,85E-02 | 8,91E-02 | 1,22E-01 | 1,18E-01 | 1,36E-01 | 1,42E-01 |
| Effective dose 60 (mSv/MBq) | 9,35E-03 | 6,04E-03 | 8,86E-03 | 1,47E-02 | 2,12E-02 | 5,21E-02 | 1,90E-02 | 7,35E-02 | 2,22E-02 | 1,15E-02 |
| Effective dose 103 (mSv/MBq) | 1,27E-02 | 5,99E-03 | 8,82E-03 | 1,27E-02 | 1,86E-02 | 3,30E-02 | 1,82E-02 | 5,02E-02 | 1,91E-02 | 1,59E-02 |

Table 5.4: Individual organ absorbed doses in mGy/MBq and effective doses in mSv/MBq.

| | TIAC (h) | | Dose (mGy/MBq) | |
|---|---|---|---|---|
| **Target organs** | **Mean** | **SD** | **Mean** | **SD** |
| Muscle | 1,70E-01 | 4,81E-02 | 4,29E-03 | 1,23E-03 |
| Cortical bone surface | 3,15E-06 | 1,40E-06 | 4,68E-03 | 1,48E-03 |
| Trabecular bone surface | 5,14E-06 | 2,28E-06 | | |
| Liver | 3,17E-02 | 1,22E-02 | 1,39E-02 | 8,55E-03 |
| Spleen | 2,80E-03 | 1,38E-03 | 1,02E-02 | 5,69E-03 |
| Kidneys | 1,65E-01 | 1,46E-01 | 1,75E-01 | 1,52E-01 |
| Pyelum | 1,34E-02 | 1,59E-02 | 2,29E-01 | 2,61E-01 |
| Stomach wall | 3,62E-05 | 4,31E-05 | 1,15E-02 | 1,21E-02 |
| Small intestine wall | 2,96E-04 | 3,10E-04 | 1,09E-02 | 7,89E-03 |
| Right colon wall | 1,13E-04 | 1,08E-04 | 6,94E-03 | 4,27E-03 |
| Left colon wall | 1,06E-04 | 1,01E-04 | | |
| Recto-sigmoid colon wall | 1,97E-05 | 5,55E-06 | 9,07E-03 | 1,87E-03 |
| Prostate | 5,13E-04 | 2,17E-04 | 2,93E-02 | 6,73E-03 |
| Heart | 4,34E-03 | 1,58E-03 | 6,87E-03 | 3,28E-03 |
| Lung | 3,84E-03 | 1,76E-03 | 3,22E-03 | 1,49E-03 |
| Thyroid | 1,49E-03 | 6,07E-05 | 4,24E-03 | 1,22E-03 |
| Oesophagus | 1,67E-06 | 3,83E-07 | 3,03E-03 | 1,90E-03 |
| Red bone marrow | 3,70E-02 | 1,91E-02 | 9,03E-03 | 3,08E-03 |
| Urinary bladder wall | 2,28E-01 | 5,22E-02 | 1,07E-01 | 2,50E-02 |
| Effective dose 60 | | | 2,38E-02 | 2,07E-02 |
| Effective dose 103 | | | 2,06E-02 | 1,24E-02 |

Table 5.5: Mean and standard deviation of the individual TIAC and absorbed doses.

| | **Mean** | **Median** | **Maximum** | **Minimum** |
|---|---|---|---|---|
| **TIAC (h)** | 2,19E-01 | 8,82E-02 | 8,94E-01 | 3,43E-03 |
| **Dose (mGy/MBq)** | 5,44E-01 | 2,19E-01 | 2,21E+00 | 8,79E-03 |

Table 5.6: Statistics of the pancreatic TIAC and absorbed dose.

## 5.4 Dosimetry estimations for [$^{177}$Lu]SB3

Estimated absorbed doses for potential organs at risk in a prostate cancer treatment with [$^{177}$Lu]SB3 (pancreas, kidneys and red bone marrow) are displayed in table 5.7 for an injected activity of 7.4 GBq, aside from the results for the intermediate calculations including the biologic and effective half-lives of the radiotracer in the target organ and its TIAC. The highest dose is expected to be achieved in the kidney pelvis, whereas the less irradiated organ would be the red bone marrow. The pancreas receives less radiation dose than the one predicted for the bombesin analog [$^{177}$Lu]-NODAGA-M19. Moreover and according to the paper published by Gnesin *et al*, the estimated pancreatic dose delivered by [$^{177}$Lu]SB3 will not produce significant toxicity, since the absorbed doses delivered in external beam radiotherapy (EBRT), which are at least superior by one order of magnitude, do not produce harmful effects either. [28] The dose to the bone marrow is not an issue, since a maximum value of 2 Gy is taken as reference from iodine-131 ($^{131}$I) procedings.[30] Regarding the kidney dose, a dose limit of 28 Gy is reported in the european guidelines for [$^{177}$Lu]DOTA-TATE, meaning that the estimated dose for [$^{177}$Lu]SB3 agrees with this reference level. [2, 31]

The absorbed dose dependence on the pancreas volume is presented in table 5.8, embracing each pancreas volume along with the average and phantom volumes. The resulting dose fluctuation (0.7 – 1.6 Gy) is not relevant and similar dose values were accomplished for the average and phantom volumes, which indicates that the phantom pancreas is a trustworthy model to predict the pancreatic uptake in this situation.

Predicting the decay of $^{177}$Lu from the $^{68}$Ga decay comes along with an error, which is described by an extra dose range in table 5.9. This range quantifies the dose expected to remain in the organ beyond the scanning time in which the study took place.

| **Target organs** | $T_{biol}$ **(h)** | $T_{eff}$ **(h)** | **TIAC (h)** | **Dose (Gy/GBq)** | **Dose per 7.4 GBq injected (Gy)** |
|---|---|---|---|---|---|
| Pancreas | 3,5 | 3,4 | 0,3 | 0,2 | 1,2 |
| Right kidney | 0,2 | 0,2 | 1,5 | 0,3 | 2,2 |
| Left kidney | 0,4 | 0,4 | | | |
| Pyelum | 0,3 | 0,3 | 0,6 | 3,0 | 22,4 |
| Red bone marrow | 0,2 | 0,2 | 0,22 | 0,01 | 0,06 |

Table 5.7: Biological half-lives, effective half-lives and TIACs in h, along with doses in Gy/GBq and total dose estimations in Gy for the organs at risk.

| Patient number | Pancreas volume (ml) | Dose per 7.4 GBq injected (Gy) |
|---|---|---|
| 1 | 146 | 0,9 |
| 2 | 114 | 0,7 |
| 3 | 172 | 1,1 |
| 4 | 174 | 1,1 |
| 5 | 144 | 0,9 |
| 6 | 189 | 1,2 |
| 9 | 170 | 1,1 |
| 10 | 247 | 1,6 |
| 11 | 139 | 0,9 |
| 12 | 135 | 0,9 |
| **Average** | **163** | **1,2** |
| **Phantom** | **174** | **1,2** |

Table 5.8: Absorbed dose in Gy for each pancreas volume (per 7.4 GBq of injected activity), including results for the average and phantom volumes.

| Target organs | Dose per 7.4 GBq injected (Gy) | Extra dose range (Gy) |
|---|---|---|
| Pancreas | 1,2 | 0,4 – 3,5 |
| Kidneys | 2,2 | 0,1 – 3,3 |
| Pyelum | 22,4 | 0,0 – 6,8 |
| Red bone marrow | 0,1 | 0,0 – 0,3 |

Table 5.9: Extra dose range expected in Gy when estimating the decay of $^{177}$Lu from the decay of $^{68}$Ga.

## 5.5 Pharmacokinetics and therapy prediction

The pharmacokinetic analysis of [$^{68}$Ga]SB3 was performed only for patients 2 and 11, due to lack of quality in the AIFs obtained for the remaining. The results for the 2-tissue compartment model fitting are displayed in figures 5.3 and 5.4 for each patient. They include the AIF and tumour uptake, as well as the model concentration curve ($C_{model}$), the concentrations of the tracer in each compartment ($C_1$ and $C_2$), and the model fitted parameters ($K_1$ to $k_4$).

In PT2 (figure 5.3), the radiotracer presents a fast kinetics, since the specific binding to the tumour becomes dominant after 36 min ($C_2$ starts exceeding $C_1$). However, $C_2$ decreases after 90 min, which suggests that therapy would not be advisable for this patient, as the specific binding will cease in a much shorter time when comparing to the half-life of $^{177}$Lu. Also, parameters $k_3$ and $k_4$ are similar, which supports this statement.

[$^{68}$Ga]SB3 shows a slower kinetics in the tumour of PT11 (figure 5.4), as $C_2$ is significantly lower than $C_1$ at early time points, which indicates that here the image signal is mostly due to the perfusion of the tumour than due to specific binding of the tracer. Specific binding becomes dominant after 170 min, which is more than twice the physical half-life of $^{68}$Ga. This suggests that imaging this tumour with SB3 labelled with $^{68}$Ga might not provide visual information of receptor binding. However, therapy may be a possibility in this case, since we expect $C_2$ to increase after 170 min and remain high for a while. Furthermore, the estimated value for $k_4$ is much lower than for $k_3$, which reinforces the former statement and implies that specific receptor binding is likely to occur within a period compatible with the half-life of $^{177}$Lu.

After selecting PT11 as a possible candidate for therapy, it was evaluated which model (1- or 2-tissue compartments) described better the pharmacokinetic behaviour of [$^{68}$Ga]SB3 in the normal prostate tissue. Figure 5.5 presents concentration curves of the 2-tissue compartment model applied to the normal prostate, along with the parameters estimated with both models (1- and 2-tissue compartments). It is clear that the healthy prostate tissue has very low specific binding, thus it is better described by a 1-tissue compartment model. These results enhance the possibility of an effective therapy with [$^{177}$Lu]SB3, since having a much higher receptor binding in the tumour than in normal prostate tissue leads to a higher radiation dose to the tumour cells while sparing the healthy ones. PT11 expected therapeutic absorbed doses per cycle with [$^{177}$Lu]SB3 are quantified in table 5.10, for a range of tumour volumes and PVE corrected. It was not possible to quantify the actual size of the tumour, thus different volumes were considered, whose upper limit was the phantom prostate volume. Since these volumes were small, they experience PVE and the absorbed doses need to be corrected with appropriate recovery coefficients [7]. The estimated therapeutic doses (PVE corrected) extend from 5.8 Gy to 14.1 Gy, which are significantly higher than the estimated absorbed dose on the normal prostate (0.1 Gy PVE corrected considering the prostate volume in the phantom).

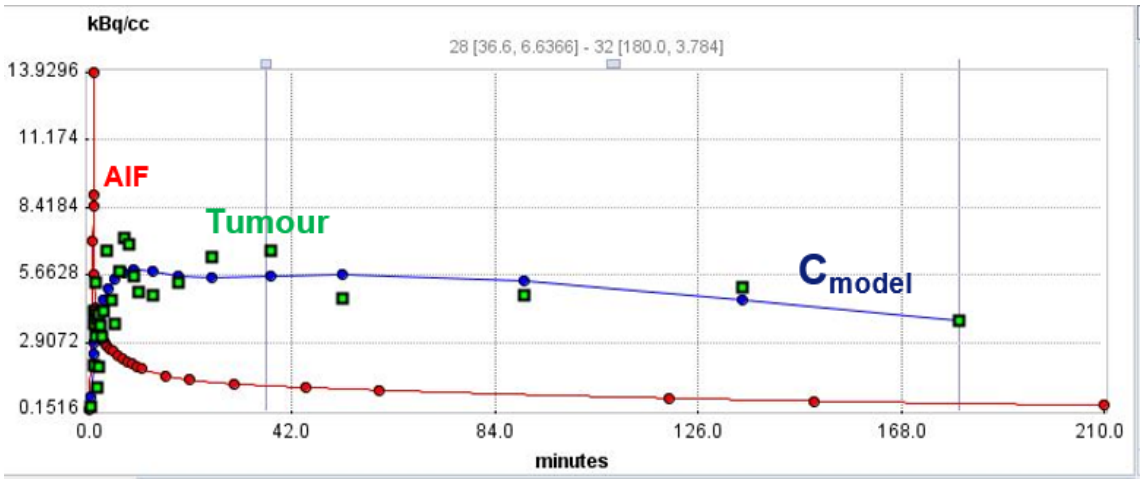


(a)

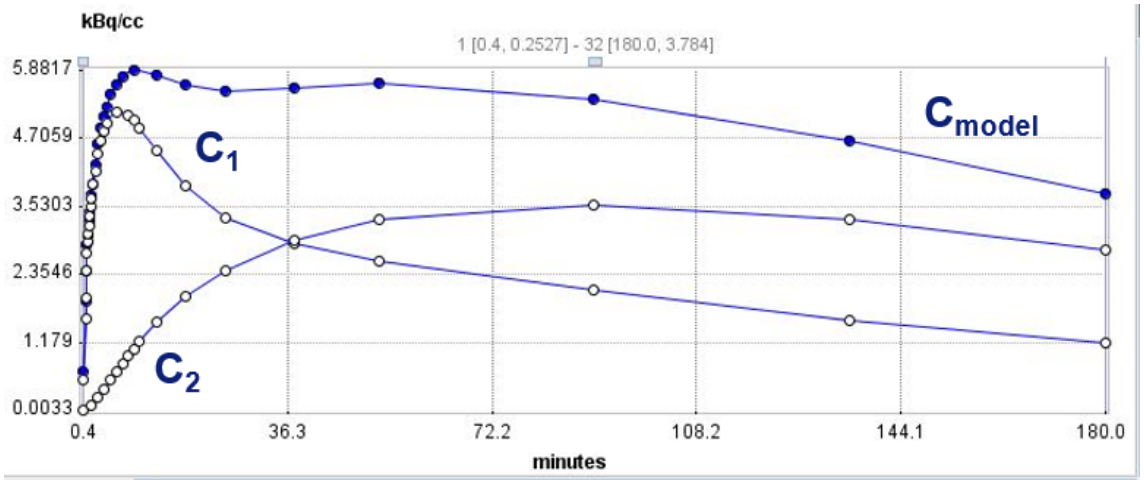


(b)

| Parameter | Current value | Unit | % SE |
|---|---|---|---|
| ☐ vB | 0.05 | 1/1 | --- |
| ☑ K1 | 0.526502 | ml/ccm/min | 13.26 |
| ☑ k2 | 0.203061 | 1/min | 32.13 |
| ☑ k3 | 0.028673 | 1/min | 77.12 |
| ☑ k4 | 0.016705 | 1/min | 72.34 |
| Vs | 4.450459 | ml/ccm | 29.98 |
| Vt | 7.043282 | ml/ccm | 19.89 |
| K1/k2 | 2.592824 | ml/ccm | 21.63 |
| k3/k4 | 1.716451 | 1/1 | 38.48 |
| Flux | 0.065145 | ml/ccm/min | 52.73 |
| LambdaK3 | 0.074343 | ml/ccm/min | 59.39 |
| ChiSquare | 30.352378 | | |

(c)

Figure 5.3: 2TCM applied in tumour of PT2: (a) Curves of uptake in the blood and tumour together with the model curve ($C_{model}$); (b) Model curve ($C_{model}$) with partial activity concentrations in both compartments ($C_1$ and $C_2$); (c) Parameters of the model with respective standard error.

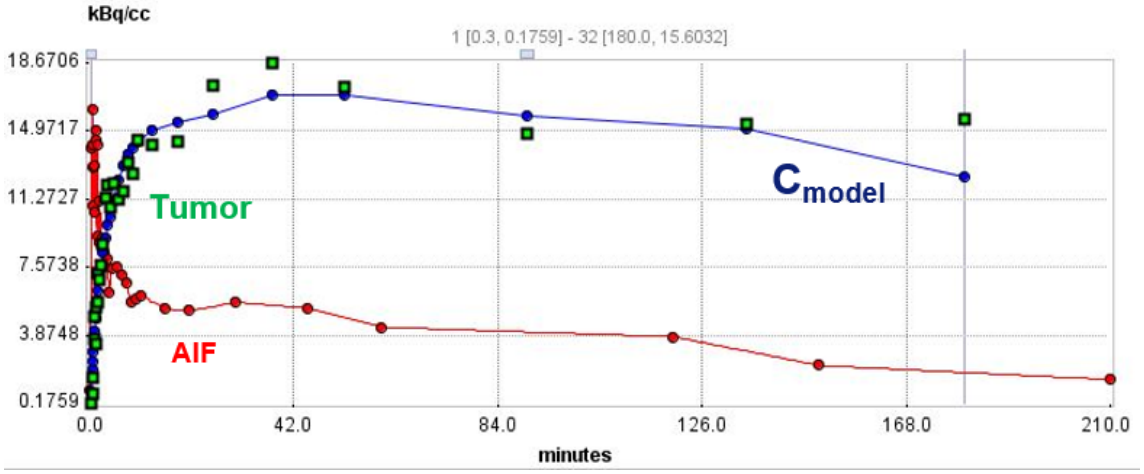


(a)

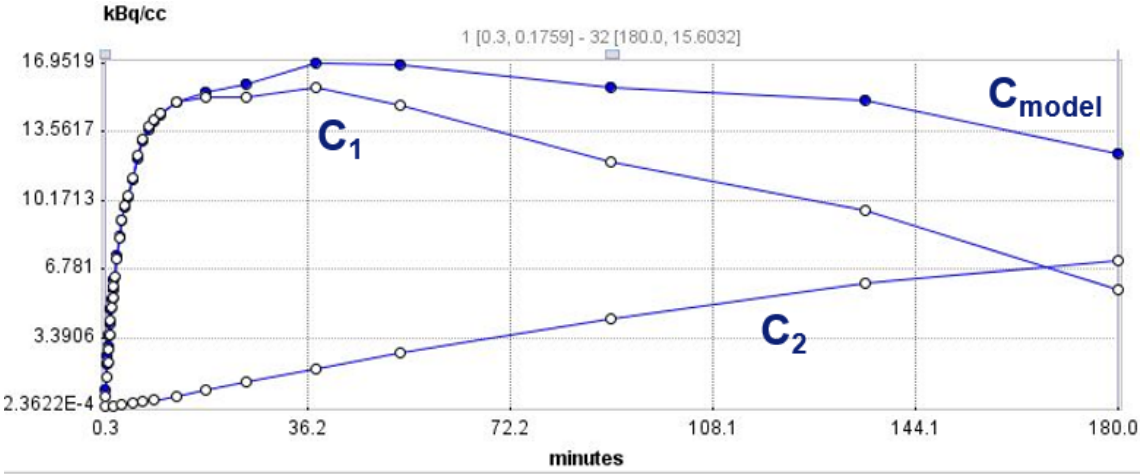


(b)

| Parameter | Current value | Unit | % SE |
|---|---|---|---|
| ☐ vB | 0.05 | 1/1 | --- |
| ☑ K1 | 0.322989 | ml/ccm/min | 6.36 |
| ☑ k2 | 0.108875 | 1/min | 13.75 |
| ☑ k3 | 0.0035 | 1/min | 88.65 |
| ☑ k4 | 1.0E-102 | 1/min | 8.87E101 |
| Vs | 1.038341E100 | ml/ccm | Infinite |
| Vt | 1.038341E100 | ml/ccm | Infinite |
| K1/k2 | 2.966591 | ml/ccm | 8.8 |
| k3/k4 | 3.500116E99 | 1/1 | Infinite |
| Flux | 0.01006 | ml/ccm/min | 78.85 |
| LambdaK3 | 0.010383 | ml/ccm/min | 81.29 |
| ChiSquare | 9.008253 | | |

(c)

Figure 5.4: 2TCM applied in tumour of PT11: (a) Curves of uptake in the blood and tumour together with the model curve ($C_{model}$); (b) Model curve ($C_{model}$) with partial activity concentrations in both compartments ($C_1$ and $C_2$); (c) Parameters of the model with respective standard error.

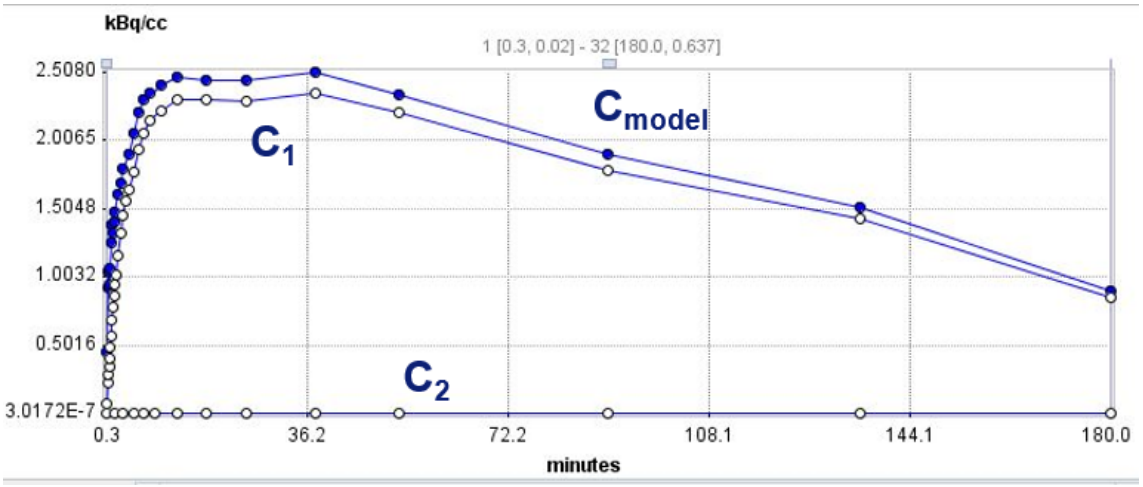


(a)

| Parameter | Current value | Unit | % SE |
|---|---|---|---|
| vB | 0.05 | 1/1 | --- |
| K1 | 0.051943 | ml/ccm/min | 317.87 |
| k2 | 0.121405 | 1/min | 20574.91 |
| k3 | 6.040039E-5 | 1/min | 2.52E9 |
| k4 | 7.510996 | 1/min | 13119.49 |
| Vs | 3.440551E-6 | ml/ccm | 2.52E9 |
| Vt | 0.427848 | ml/ccm | 17.76 |
| K1/k2 | 0.427844 | ml/ccm | 20257.82 |
| k3/k4 | 8.041595E-6 | 1/1 | 2.52E9 |
| Flux | 2.582911E-5 | ml/ccm/min | 2.52E9 |
| LambdaK3 | 2.584197E-5 | ml/ccm/min | 2.52E9 |
| ChiSquare | 147.738597 | | |

(b)

| Parameter | Current value | Unit | % SE |
|---|---|---|---|
| vB | 0.05 | 1/1 | --- |
| K1 | 0.052458 | ml/ccm/min | 21.7 |
| k2 | 0.123264 | 1/min | 32.14 |
| Vt | 0.425572 | ml/ccm | 16.64 |
| ChiSquare | 137.93501 | | |

(c)

Figure 5.5: Pharmacokinetics of normal prostate of PT11: (a) and (b) show the model curve ($C_{model}$) with partial activity concentrations in both compartments ($C_1$ and $C_2$) and the parameters when using a 2TCM; (c) Parameters when applying a 1TCM.

However, the predicted absorbed doses may not be enough to treat the tumour, since a radionuclide therapy with [$^{177}$Lu]PSMA, which is currently under clinical validation, yields around 97 Gy per 7.4 GBq injected (1 cycle) to treat the tumour. [2]

An attempt to perform pharmacokinetic analysis with PT6 data made us realize the importance of data quality, mainly regarding the IDIF. Figure 5.6 shows the fitted AIF, along with the estimated 2TCM parameters for PT6. As can be observed, the data points are strongly scatted in the peak area, which leads to a poorly fitted AIF. Therefore, the estimated model parameters are unrealistic, since they suggest that the tracer unbinds faster than the specific binding occurs ($k_3$ significantly lower than $k_4$) and large standard errors are associated to those parameters. In the interest of improving data quality and ensuring that pharmacokinetic modelling is a reasonably accurate method to predict therapy response of each patient, it is advisable to obtain an AIF based on blood sample measurements, instead of being image derived.

The interpretation of these results assumes that SB3 remains stable on the blood-

stream, which was already verified in a previous study. [5] Therefore, metabolyte blood analysis will not be required for a better estimation, which is an advantage.

| **Tumour volume (ml)** | **Recovery coefficient** | **Dose per 7.4 GBq injected (Gy)** | **Dose PVE corrected (Gy)** |
|---|---|---|---|
| 0,5 | 0,33 | 4,7 | 14,1 |
| 1 | 0,50 | 4,7 | 9,4 |
| 3 | 0,69 | 4,7 | 6,9 |
| 5 | 0,71 | 4,8 | 6,7 |
| 7 | 0,74 | 4,8 | 6,4 |
| 10 | 0,78 | 4,8 | 6,1 |
| 12 | 0,80 | 4,8 | 6,0 |
| 14 | 0,81 | 4,8 | 5,9 |
| 16 | 0,82 | 4,8 | 5,9 |
| 17,8 | 0,83 | 4,8 | 5,8 |

Table 5.10: Absorbed doses to the tumour of PT11 (with and without PVE correction) depending on tumour volume and the recovery coefficient.

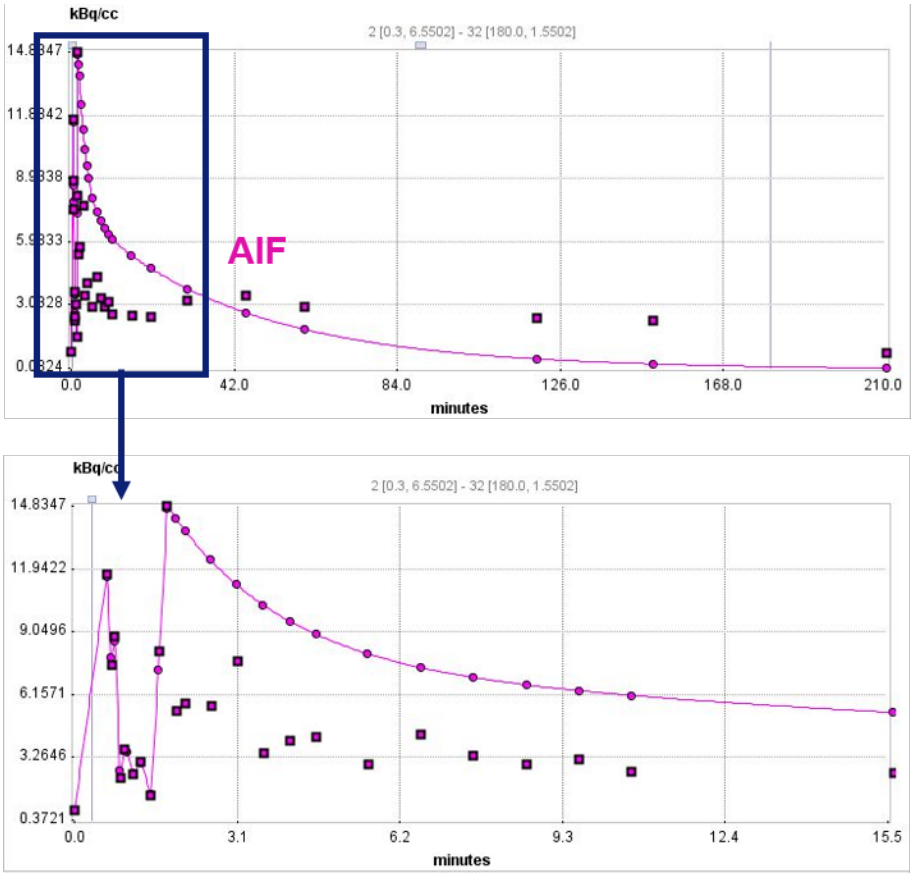


Figure 5.6: Scattered AIF of PT6.

# 6 Conclusion and future work

The effective dose of [$^{68}$Ga]SB3 is 13 $\mu$Sv/MBq, which is similar to the doses of the most common PET radiopharmaceuticals used at the present time. The organs with the highest uptake of the radiotracer are the pancreas (198 $\mu$Gy/MBq), the kidney pelvis (133 $\mu$Gy/MBq) and the urinary bladder (113 $\mu$Gy/MBq).

In a therapeutic context, the estimated [$^{177}$Lu]SB3 absorbed doses for the potential organs at risk (pancreas, kidneys and red bone marrow) are not expected to produce significant toxicity, since agreement with established dose limits was verified. In this group of patients, the pancreatic absorbed dose did not show a significant dependence on the pancreas volume and the phantom pancreas demonstrated to be a trustworthy model to predict the pancreatic uptake. The pancreas volume is considered an important parameter when the therapy provides doses around 40 Gy and the patient has a smaller pancreas volume than average. However, this is not the case, since the estimated pancreatic dose is around 5 Gy, which is relatively low.

In the present work, compartmental modelling proved to be a powerful tool to select the patients for $^{177}$Lu therapy based on the $^{68}$Ga images, since the activity concentration in each compartment and rate constants of the models provided valuable information on the binding properties of the tracer. Therefore, this method offers a possibility to achieve a personalized medicine approach, discarding the candidates that would not benefit from this treatment and sparing them from unnecessary radiation exposure.

Patient 2 turned out to be not a good candidate for therapy, as the [$^{68}$Ga]SB3 specific binding starts decreasing after 90 min. On the other hand, the kinetic behaviour of the imaging tracer in the tumour of patient 11 shows that the specific binding gradually increases, becoming dominant after 170 min. From this scenario, it can be stated that this patient would benefit from the treatment, although the exact behaviour of the [$^{177}$Lu]SB3 within a week time is not predictable. At this point, estimation of the $^{177}$Lu delivered dose to the tumour would dictate the final decision on the selection for therapy. Unfortunately, a estimated maximum absorbed dose of 14.1 Gy to the tumour (per cycle) was found, which may not be enough for its erradication. Two solutions for this issue would be increasing the number of cycles and/or administrate a higher activity of $^{177}$Lu. However, the number of cycles might be affected by the cumulative dose limit for the organs at risk. Overall, this analysis also demonstrates the importance of performing pre-treatment dosimetry.

It should be noted that an overall conclusion regarding the possibility of using [$^{177}$Lu]SB3 as a therapeutic agent for primary stage of prostate cancer was not reached, since it was only possible to perform the pharmacokinetic analysis based on the imaging data from two of the patients. However, the results from this work show the potential of the compartment modelling in a particular case and enhance the importance of performing dosimetry studies before submitting the patients to radionuclide therapy procedures.

Since it was demonstrated that the compartment modelling method depends strongly

on the quality of AIF, one possible way to reduce the scattering in these curves is to use an AIF based on blood sample measurements, instead of being image derived. This modification is expected to optimize the analysis of the data from a certain group of patients. On the other hand, this solution is not suitable in practice, as it results in a very painful procedure for the patients.

Over the coming years, the application of [$^{68}$Ga]SB3 in diagnosing primary prostate cancer patients, suspected for lymph node metastases, might be evaluated to see if the lymph node metastases are detected in the images. This might be an alternative diagnosis which spares the patients to lymph node dissection and, more importantly, it offers the possibility of guiding the urologist in deciding whether and where to take tissue punction samples for pathologic analysis. The same analysis shown in this work might be helpful in investigating the possibility of employing radionuclide therapy procedures to directly erradicate the lymph node tumours. Moreover, the same clinical analysis may also be valuable in assessing the dosimetry and kinetic behaviour of other GRPR antagonists like NeoBOMB1 and study the possibility of a theranostics approach.[32] At last instance, the potential of using SB3 for pre- and intra-operative imaging of prostate cancer is curretly under investigation.[33]

# References

[1] A. Yordanova, E. Eppard, S. Kürpig, R. A. Bundschuh, S. Schönberger, M. Gonzalez-Carmona, G. Feldmann, H. Ahmadzadehfar, and M. Essler. Theranostics in nuclear medicine practice. *OncoTargets and Therapy*, 10:4821–4828, 2017.

[2] EANM and UEMS/EBNM. European Nuclear Medicine Guide, 2018. https://www.nucmed-guide.app/#!/startscreen.

[3] B. T Ristau, D. S. O'Keefe, and D. J. Bacich. The prostate-specific membrane antigen: lessons and current clinical implications from 20 years of research. *Urology Oncology: Seminars and Original Investigations*, 32(3):272–279, 2015.

[4] C. Kratochwil, W. P. Fendler, M. Eiber, R. Baum, M. F. Bozkurt, J. Czernin, R. C. D. Bolton, S. Ezziddin, F. Forrer, R. J. Hicks, T. A. Hope, L. Kabasakal, M. Konijnenberg, K. Kopka, M. Lassmann, F. M. Mottaghy, W. Oyen, K. Rahbar, H. Schöder, I. Virgolini, H.-J. Wester, L. Bodei, S. Fanti, U. Haberkorn, and K. Herrmann. EANM procedure guidelines for radionuclide therapy with 177Lu-labelled PSMA-ligands ($^{177}$Lu-PSMA-RLT). *Eur J Nucl Med Mol Imaging*, 2019.

[5] T. Maina, H. Bergsma, H. R. Kulkarni, D. Mueller, D. Charalambidis, E. P. Krenning, B. A. Nock, M. de Jong, and R. P. Baum. Preclinical and first clinical experience with the gastrin-releasing peptide receptor-antagonist [$^{68}$ga]SB3 and PET/CT. *Eur J Nucl Med Mol Imaging*, 43(5):964–973, 2015.

[6] Laboratoire National Henri Becquerel. Nuclear data table. http://www.lnhb.fr/nuclear-data/nuclear-data-table/.

[7] A. Sanchez-Crespo. Comparison of Gallium-68 and Fluorine-18 imaging characteristics in positron emission tomography. *Applied Radiation and Isotopes*, 76:55–62, 2013.

[8] S. R. Cherry, J. A. Sorenson, and M. E. Phelps. *Physics in Nuclear Medicine*. Fourth edition.

[9] Siemens (Erlangen, Germany). Biograph mCT brochure, 2018. https://www.siemens-healthineers.com/molecular-imaging/pet-ct/biograph-mct#ADD_INFO.

[10] Perkin Elmer (Massachusetts, USA). Perkin Elmer WIZARD 1480 automatic gamma counter information. http://www.bilmar.com.tr/PDF/PERKIN%20ELMER/Gamma%20Counter.pdf.

[11] International Commission on Radiological Protection. 1990 Recommendations of the International Commission on Radiological Protection. ICRP Publication 60.

[12] International Commission on Radiological Protection. The 2007 Recommendations of the International Commission on Radiological Protection. ICRP Publication 103.

[13] International Commission on Radiological Protection. Basic Anatomical and Physiological Data for Use in Radiological Protection: Reference Values. ICRP Publication 89.

[14] W. E. Bolch, K. F. Eckerman, G. Sgouros, and S. R. Thomas. MIRD Pamphlet No. 21: a generalized schema for radiopharmaceutical dosimetry - standardization of nomenclature. *J Nuc Med*, 50(3):477–484, 2009.

[15] D. L. Bailey, J . L. Humm, A. Todd-Pokropek, and A. van Aswegen. *Nuclear Medicine Physics, a handbook for teachers and students*.

[16] S. R. Thomas, M. G. Stabin, C.-T. Chen, and R. C. Samaratunga. MIRD Pamphlet No. 14: a dynamic urinary bladder model for radiation dose calculations. *J Nuc Med*, 33(5):783–802, 1992.

[17] Y. Kimura M. Naganawa M. Shidahara H. Watabe, Y. Ikoma. PET kinetic analysis - compartmental model. *Ann Nucl Med*, 20(9):583–588, 2006.

[18] PMOD Technologies LLC. PMOD kinetic modeling (PKIN) user manual, version 4.0, 2018. http://www.pmod.com.

[19] International Commission on Radiological Protection. Radiation Dose to Patients from Radiopharmaceuticals: A Compendium of Current Information Related to Frequently Used Substances. ICRP Publication 128.

[20] M. Andersson, L. Johansson, K. Eckerman, and S. Mattsson. IDAC-Dose 2.1, an internal dosimetry program for diagnostic nuclear medicine based on the ICRP adult reference voxel phantoms. *EJNMMI research*, 7(1):88, 2017.

[21] International Commission on Radiological Protection. The ICRP Computational Framework for Internal Dose Assessment for Reference Adults: Specific Absorbed Fractions. ICRP Publication 133.

[22] M. G. Stabin, R. B. Sparks, and E. Crowe. OLINDA/EXM: The Second-Generation Personal Computer Software for Internal Dose Assessment in Nuclear Medicine. *J Nucl Med*, 46:1023–1027, 2005.

[23] F. E. Grubbs. Procedures for Detecting Outlying Observations in Samples. *Technometrics*, 11(1):1–21, 1969.

[24] G. Glatting, P. Kletting, S. N. Reske, K. Hohl, and C. Ring. Choosing the optimal fit function: comparison of the Akaike information criterion and the F-test. *Medical Physics: The International Journal of Medical Physics Research and Practice*, 34(11):4285–4292, 2007.

[25] C. Hindorf, G. Glatting, C. Chiesa, O. Lindén, and G. Flux. EANM Dosimetry Committee guidelines for bone marrow and whole-body dosimetry. *Eur J Nucl Med Mol Imaging*, 37(6):1238–1250, 2010.

[26] RADAR. Medical Procedure Radiation Dose Calculator. https://doseinfo-radar.com/RADARDoseRiskCalc.html.

[27] A. Dash, M. R. A. Pillai, and F. F. Knapp Jr. Production of $^{177}$Lu for Targeted Radionuclide Therapy: Available Options. *Nucl Med Mol Imaging*, 49:85–107, 2015.

[28] S. Gnesin, F. Cicone, P. Mitsakis, A. van der Gucht, S. Baechler, R. Miralbell, V. Garibotto, T. Zilli, and J. O. Prior. First in-human radiation dosimetry of the gastrin-releasing peptide (GRP) receptor antagonist $^{68}$Ga-NODAGA-MJ9. *EJNMMI research*, 8:8–108, 2018.

[29] I. Bakker. Clinical trial with Sarabesin 3, a GRP receptor antagonist, labelled with gallium-68, in patients with prostate cancer confined to the primary organ. SB3 Status Report.

[30] R. S. Benua, N. R. Cicale, M. Sonenberg, and R. W. Rawson. The relation of radioiodine dosimetry to results and complications in the treatment of metastatic thyroid cancer. *The American journal of roentgenology, radium therapy and nuclear medicine*, 87:171–82, 1962.

[31] H. Bergsma, M. W Konijnenberg, W. A. van der Zwan, B. L. R. Kam, J. J. M. Teunissen, P. P. Kooij, K. A. L. Mauff, E. P. Krenning, and D. J. Kwekkeboom. Nephrotoxicity after PRRT with $^{177}$Lu-DOTA-octreotate.

[32] S. U. Dalm, I. L. Bakker, E. de Blois, G. N. Doeswijk, M. W. Konijnenberg, F. Orlandi, D. Barbato, M. Tedesco, T. Maina, B. A. Nock, and M. de Jong. $^{68}$Ga/$^{177}$Lu-NeoBOMB1, a Novel Radiolabeled GRPR Antagonist for Theranostic Use in Oncology. *EJNMMI research*, 58:293–299, 2017.

[33] I. L. Bakker, S. T. van Tiel, J. Haeck, G.N. Doeswijk, E. de Blois, M. Segbers, T. Maina, B. A. Nock, M. de Jong, and S. U. Dalm. In Vivo Stabilized SB3, an Attractive GRPR Antagonist, for Pre- and Intra-Operative Imaging for Prostate Cancer. *EJNMMI research*, 20:973–983, 2018.

[34] G. B. Saha. *Physics and Radiobiology of Nuclear Medicine*. Third edition.

[35] J. J. M. Kouwenberg. Pharmacokinetics and Dosimetry of Gallium-68 labelled Sarabesin 3 for Prostate Cancer, 2015. Master Thesis (Delft University of Technology, Erasmus Medical Center.